

Velocity obstacle based local collision avoidance for a holonomic elliptic robot

Beom H. Lee^{1,2} · Jae D. Jeon^{1,2} · Jung H. Oh^{1,2}

Received: 21 June 2015 / Accepted: 24 May 2016 / Published online: 9 June 2016
© Springer Science+Business Media New York 2016

Abstract This paper addresses the local collision avoidance problem for a holonomic elliptic robot, where its footprint and obstacles are approximated with the minimum area bounding ellipses. The proposed algorithm is decomposed into two phases: linear and angular motion planning. In the former phase, the ellipse-based velocity obstacle is defined as a set of all linear velocities of the robot that would cause a collision with an obstacle within a finite time horizon. If the robot's new linear velocity is selected outside of the velocity obstacle, the robot can avoid the obstacle without rotation. In the latter phase, the angular velocity is selected at which the robot can circumvent the obstacle with the minimum possible deviation by finding the collision-free rotation angles and the preferred angular velocities. Finally, the performance of the suggested algorithm is demonstrated in simulation for various scenarios in terms of travel time, distance, and the number of collisions.

Keywords Collision avoidance · Holonomic robot · Ellipse · Motion planning · Dynamic environment

1 Introduction

Collision-free motion planning has been one of the fundamental problems in robotics, which is hierarchically decomposed into two parts: high-level and low-level planners (Alonso-Mora et al. 2015). The higher level planner generates the shortest path to the goal using A* or Dijkstra's algorithm from distance graphs based on the global environment information, whereas the local level planner modifies the path from the higher level one by considering unexpected dynamic obstacles and motion constraints of mobile robots. This paper deals with the latter, where a robot selects its new linear and angular velocities in each sense-plan-act cycle.

In the local collision avoidance problem in the 2D plane, robots and obstacles are approximated by simple geometric objects since the contours of them are quite complicated in general. There are three criteria in choosing a bounding box: tightness, computational ease, and complexity of describing shape. The first criterion is that the area of the bounding box should be as low as possible. If the tightness is not satisfied, a robot has to travel longer paths than necessary to avoid obstacles and is not allowed to pass an alley even though it is possible in practice. The second criterion is that the collision avoidance conditions should be calculated simply and fast. Because the collision avoidance has to be guaranteed while a robot performs complicated tasks, the algorithm should utilize just a little part of the computational resources. The final criterion is to reduce the amount of information used to store a computer model (Goerzen et al. 2010). With compact representation of the shape, a robot can not only improve the running time for planning a collision-free path but also model the shape of a newly detected obstacle by equipped sensors without the risk of overfitting.

In general, both circles and polygons have been typical candidates for enclosing objects due to its simplicity in colli-

✉ Jae D. Jeon
innocent88@snu.ac.kr

Beom H. Lee
bhlee@snu.ac.kr

Jung H. Oh
bulley85@snu.ac.kr

¹ Department of Electrical and Computer Engineering, Seoul National University, 1 Gwanak-ro, Gwanak-gu, Seoul, Republic of Korea

² Automation and Systems Research Institute, Seoul National University, 1 Gwanak-ro, Gwanak-gu, Seoul, Republic of Korea

sion detection. For example, a collision between two circles (or polygons) is equivalent to that between a point and an inflated circle (or polygon) in the configuration space (C-space) introduced in [Lozano-Pérez \(1983\)](#). Then it is easy to test the inclusion of the point in the configuration space obstacle (C-obstacle). However, there is a trade-off between the tightness and the complexity. While it is specified by just three variables (x-position, y-position, and radius), the bounding circle becomes overly conservative if an object is elongated. To remedy this problem, some authors approximated the object by a group of several circles in [Chakravarthy and Ghose \(1998\)](#), [Fiorini and Shiller \(1998\)](#), and [Takahashi et al. \(2013\)](#). In case of the bounding polygon, the convex hull of the object may satisfy the tightness, but the complexity increases as much as twice of the number of the vertices.

In this respect, approximating an object with the minimum area bounding ellipse, known as the Löwner-John ellipses ([John 2014](#)), compromises between these two criteria. [Choi et al. \(2006\)](#) and [Chakravarthy and Ghose \(2011\)](#) have stated that far fewer ellipses than circles are required to enclose a given object with the same degree of the tightness. Also, an ellipse is characterized by five variables (x-position, y-position, major radius, minor radius, and orientation), which is lower than that of the simplest polygon—an triangle. However, collision detection between ellipses is more difficult than those between circles and between polygons.

Some researchers have focused on calculating the distance between two ellipses. [Miloh \(1983\)](#) measured the distance along the common normal to both of them to solve a differential game of two elliptic ships, which is a maritime collision avoidance problem. [Rimon and Boyd \(1997\)](#) showed that the distance between two ellipses could be computed as an eigenvalue problem. In addition, it was calculated by intersecting the Plücker images of their normal congruences as introduced in [Sohn et al. \(2002\)](#). Furthermore, [Lennerz and Schomer \(2002\)](#) reduced the problem of calculating the distance to that of solving univariate polynomials of a degree of 16. In [Ju et al. \(2001\)](#), the criterion for collision detection between two convex polyhedra was proposed by estimating the distance with the enclosing ellipsoid and the enclosed ellipsoid. On the other hand, other researchers have suggested algebraic conditions for the separation between two ellipses without calculating the distance in [Wang et al. \(2001, 2004\)](#), [Etayo et al. \(2006\)](#), [Choi et al. \(2006, 2009\)](#), and [Jia et al. \(2011\)](#). They have shown that two ellipses are separate if and only if their characteristic equation has two distinct positive roots.

To plan a collision-free path for an elliptic robot, it is convenient to map an elliptic obstacle into the C-space. For a fixed orientation, [Zheng and Palfy-Muhoray \(2007\)](#) calculated the C-obstacle by transforming an ellipse into a unit circle by anisotropic scaling. Our previous work ([Jeon and Lee 2014](#)) also derived it by finding the locus of the positions

of the robot touching the obstacle externally. With rotation, the C-obstacle is a 3D column structure whose cross section corresponds to the one for a particular orientation.

Collision-free motion of a robot in the presence of moving obstacles has been planned by adding the time dimension to the C-space. [Fujimura and Samet \(1989\)](#) introduced the accessibility graph method in a 2D C-space by defining the collision front, the sets of points that are accessible by the robot moving at maximum speed, and linking the points to construct a path to the goal. In addition, this method was extended to 3D environments in [Fujimura and Samet \(1993\)](#). However, since the accessibility graph is applied only in the case that C-obstacles are polyhedra, it is inappropriate to collision avoidance between ellipses.

Other studies have dealt with first-order methods that a robot avoid collisions with obstacles by selecting its velocity outside the forbidden region. In [Chakravarthy and Ghose \(1998, 2011\)](#), they first derived a necessary and sufficient condition for a collision between two arbitrary objects without superposing the shape of one object on the other, inspired from the guidance theory in the aerospace literature. This approach defined the collision cone as a set of rays starting at the origin with the direction along which a robot collided with an obstacle when they traveled at constant speeds. Although the sector angle of the cone varied depending on the robot's speed, they showed that the cone represented in the relative velocity space was invariant. In this sense, [Fiorini and Shiller \(1998\)](#) defined the velocity obstacle (VO) by translating the collision cone in the relative velocity space by the velocity of an object. The concept of VO was extended into the reciprocal velocity obstacle (RVO) and the optimal reciprocal collision avoidance (ORCA) to solve the problem in multi-robot systems ([Van Den Berg et al. 2008, 2011](#)).

Although the above algorithms did not consider the angular motion, the subsequent work such as [Giese et al. \(2014\)](#), [Jeon and Lee \(2014\)](#), and [Karamouzas and Guy \(2015\)](#) conducted researches on the collision avoidance of anisotropic robots with rotation. In [Giese et al. \(2014\)](#), the concept of reciprocally-rotating velocity obstacle (RRVO) was introduced to solve the problem of the deadlock in ORCA, emerged when polygonal robots tried to avoid collisions without rotation. The RRVO approach found the range of reachable orientations by discretizing the set of rotations of the robot. For each of the orientations, a new linear velocity was calculated by constructing the VO from the swept areas the robot may rotate through. By ordering all the potential new orientation-velocity pairs, the robot selected the optimal one. Because it employed a brute-force search strategy, the performance of the algorithm depended on the number of discretized rotation intervals.

On the other hand, [Karamouzas and Guy \(2015\)](#) suggested the formation velocity obstacles (FVO), where the orientation of a formation was aligned to the direction of motion. They

assumed that the group of robots was enclosed by the rectangular box that instantaneously rotated to lie along its velocity. While the FVOs induced by static obstacles had a closed form expression, the ones induced by dynamic obstacles were quite complicated. Hence, it was necessary to calculate the range of the velocities that would lead to a collision for all orientations separately.

Our previous work (Jeon and Lee 2014) derived the VO for an elliptic robot, named Ellipse-based Velocity Obstacle (EBVO), and showed that the robot could reach the goal with a less traveled path by controlling the rotary motion. This approach first selected the linear velocity with the EBVO, and then calculated the angular velocity proportional to the change rate of the boundary line of the EBVO with respect to the orientation of the robot. However, since the robot's angular velocity was depending on the user-defined parameter, the robot oscillated or collided with obstacles at worst if the parameter was set in the wrong way.

The proposed paper complements the analysis and remedies the problem of our previous research. By discarding the strategy based on the user-defined parameter and presenting a new strategy for the angular motion planning, an elliptic robot can avoid obstacles more safely and efficiently. In summary, the main contributions of the present work are the following: (1) the mathematical derivation of the EBVO and the process of selecting the new linear velocity are described in detail; (2) the strategy for selecting the angular velocity with which the robot can circumvent the obstacle blocking the path to the goal with the minimum deviation is presented; (3) the proposed method was validated in three scenarios in terms of travel time, distance, and the number of collisions.

The rest of this paper is organized as follows. We define the local collision avoidance problem for an elliptic robot and decompose the problem into two sub-problems in Sect. 2. In Sect. 3, it is proven that the EBVO is bounded by three lines. How to select the robot's new linear velocity is also explained. Section 4 presents the angular motion control strategy, making the robot to avoid obstacles with a less traveled path. In Sect. 5, we present the simulation results of three scenarios. Finally, this paper is concluded in Sect. 6.

2 Problem definition

We deal with the problem of real-time local collision avoidance for an elliptic robot, where the robot makes a detour to reach the goal without collisions with static or dynamic obstacles.

Consider an elliptic robot \mathcal{R} and n obstacles moving in a planar workspace \mathcal{W} , as shown in Fig. 1. The robot's shape is represented by a symmetric positive definite matrix $\mathbf{S}_{\mathcal{R}} \in \mathbb{R}^{2 \times 2}$ whose eigenvalues are squares of the semi-axes and eigenvectors indicate the principal axes. Also, the

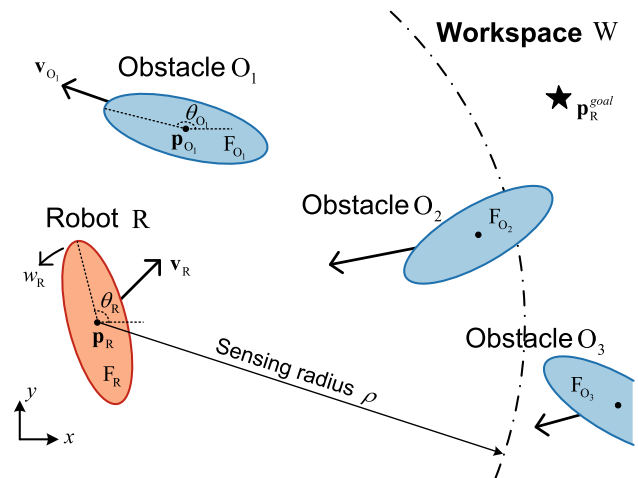


Fig. 1 An elliptic robot \mathcal{R} and obstacles \mathcal{O}_i , $i = 1, \dots, 3$ in the workspace \mathcal{W} . The robot can sense the obstacles within the range of ρ : \mathcal{O}_1 and \mathcal{O}_2 . The objective of the robot is to arrive at $\mathbf{p}_{\mathcal{R}}^{\text{goal}}$ without collisions with the obstacles

robot's configuration consists of its position $\mathbf{p}_{\mathcal{R}} \in \mathbb{R}^2$ and orientation $\theta_{\mathcal{R}} \in (-\pi, \pi]$ since it has a holonomic and omni-directional movable ability. The position $\mathbf{p}_{\mathcal{R}}$ is the center of the ellipse, and the orientation $\theta_{\mathcal{R}}$ is the angle between the major axis and the x -axis. Let f be a function given by

$$f(\mathbf{x}; \mathbf{S}, \mathbf{p}) = (\mathbf{x} - \mathbf{p})^T \mathbf{S}^{-1} (\mathbf{x} - \mathbf{p}) - 1. \quad (1)$$

The robot's footprint $\mathcal{F}_{\mathcal{R}}$, the occupied region of its work space, is defined by $\mathcal{F}_{\mathcal{R}} = \{\mathbf{x} | f(\mathbf{x}; \mathbf{S}_{\mathcal{R}}, \mathbf{p}_{\mathcal{R}}) \leq 0\}$. In addition, the robot's motion is controlled by its linear velocity $\mathbf{v}_{\mathcal{R}}$ and angular velocity $w_{\mathcal{R}}$. These two factors satisfy its dynamic constraints such as the maximum linear speed $v_{\mathcal{R}}^{\text{max}}$, angular speed $w_{\mathcal{R}}^{\text{max}}$, linear acceleration $a_{\mathcal{R}}^{\text{max}}$, and angular acceleration $\alpha_{\mathcal{R}}^{\text{max}}$.

Not only these constraints but also the set of obstacles $\{\mathcal{O}_1, \mathcal{O}_2, \dots, \mathcal{O}_n\}$ limits the robot's motion. The information of the obstacles is measured or extracted by the robot \mathcal{R} equipped with an omni-directional range sensor with a detection range up to ρ . The obstacles are assumed to move in straight lines without rotation because it is difficult to measure the angular velocity without the exact knowledge of the obstacles' shape. Therefore, for each of the observed obstacle \mathcal{O}_i , the robot tracks both the position $\mathbf{p}_{\mathcal{O}_i}$ and the linear velocity $\mathbf{v}_{\mathcal{O}_i}$ and gathers the sensor data about the outline after it was first detected. Then the shape represented by a symmetric positive definite matrix $\mathbf{S}_{\mathcal{O}_i}$ is regarded as the minimum area enclosing ellipse of the accumulated points. If the obstacle is rotating, it would be bounded by a circle whose radius is the maximum distance from the center to the boundary. In addition, the orientation $\theta_{\mathcal{O}_i}$ and its footprint $\mathcal{F}_{\mathcal{O}_i}$ is defined analogously to the robot.

In view of the fact that the sensor data is returned at a certain sampling period Δt , a discrete-time robot model is

employed. At each time instant, the robot selects its new linear velocity $\mathbf{v}_{\mathcal{R}}^{new}$ and angular velocity $w_{\mathcal{R}}^{new}$ that guarantee no collision with obstacles within a time horizon $\tau \geq 0$. Moreover, these new velocities are taken as close as possible to its preferred linear velocity $\mathbf{v}_{\mathcal{R}}^{pref}$ and angular velocity $w_{\mathcal{R}}^{pref}$ within the dynamic constraints, respectively.

When the robot's goal located at $\mathbf{p}_{\mathcal{R}}^{goal}$ is given by an external global planner, $\mathbf{v}_{\mathcal{R}}^{pref}$ has a magnitude of the robot's preferred linear speed $v_{\mathcal{R}}^{pref}$ and is directed toward $\mathbf{p}_{\mathcal{R}}^{goal}$. The preferred angular velocities, however, are affected by the obstacles in the detection area D . If they block the robot's straight path to the goal, $w_{\mathcal{R}}^{pref}$ is computed to reach the optimal orientation that enables the robot to potentially circumvent them with the minimum possible deviation. Otherwise, the robot does not need to turn around, that is $w_{\mathcal{R}}^{pref} = 0$.

Based on the above descriptions, the problem to be solved in this paper is defined as follows.

Problem 1 (*Collision avoidance for an elliptic robot*) At each time instant, compute the new linear velocity $\mathbf{v}_{\mathcal{R}}^{new}$ and angular velocity $w_{\mathcal{R}}^{new}$ of an elliptic robot \mathcal{R} in order to generate a trajectory to the goal that circumvents obstacles with the minimum possible deviation from

- (a) the measurements of the obstacles in the robot's detection area D ,
- (b) the robot's goal position $\mathbf{p}_{\mathcal{R}}^{goal}$.

However, it is infeasible to find both the optimal $\mathbf{v}_{\mathcal{R}}^{new}$ and $w_{\mathcal{R}}^{new}$ at the same time with a high enough sampling rate to be used for practical real-time applications. That is because it requires the construction of 3D C-space by convolving the footprints of obstacles and the robot at each orientation, which takes much computation time. Hence, we decompose Problem 1 into two sub-problems: Problems 2 and 3. The linear motion of the robot is determined in Problem 2, and the angular one is determined in Problem 3.

Problem 2 (*Collision avoidance for an elliptic robot that is capable of only translational motion*) Identical to Problem 1 except that $w_{\mathcal{R}}^{new} = 0$ is assumed.

Problem 3 (*Angular motion control for an elliptic robot circumventing an obstacle*) Compute the new angular velocity $w_{\mathcal{R}}^{new}$ of an elliptic robot \mathcal{R} moving at $\mathbf{v}_{\mathcal{R}}$ in order to potentially circumvent an obstacle, interrupting the robot's path to the goal, with the minimum deviation without collisions.

At each time step, Problems 2 and 3 are sequentially solved. In Problem 2, the safe linear velocity closest to the preferred one is calculated without rotation of the robot. If there is no obstacle between the robot and its goal, the new

velocity is selected as the preferred one. Otherwise, the robot moves toward the tangent direction of some obstacle to avoid collisions. In Problem 3, the robot first calculates the preferred angular velocities with which the robot potentially circumvent the obstacle with the minimum deviation. And then it selects the angular velocity closest to the preferred ones and guaranteeing no collision. After the robot rotates with the new angular velocity, it can construct a shorter path than the preceding time instant, which is not the optimal since the current orientation was determined based on the position at the preceding instant. Although it leads some lag in the linear motion planning, the decomposition yields reasonable results with a high enough sampling rate as compared with Problem 1.

3 Ellipse-based velocity obstacles

In this section, we address Problem 2, where the objective is to compute the new linear velocity of a non-rotating elliptic robot that guarantees no collision with obstacles. To solve this problem, the concept of the VO for an elliptic robot, named EBVO, is reviewed (see Jeon and Lee 2014 for further discussion). We derive the C-obstacle with respect to the robot and its tangent line equations at first. Next, it is shown that the VO of an elliptic robot induced by an elliptic obstacle with a finite time horizon can be represented by three linear inequalities. Finally, a strategy for selecting the new linear velocity is presented accounting for its dynamic constraints.

3.1 Configuration space obstacle

For the collision free motion planning, the robot \mathcal{R} and the obstacle \mathcal{O} are mapped from workspace \mathcal{W} to the robot's configuration space \mathcal{Q} , which is the space of all possible configurations of the robot. The C-space \mathcal{Q} is a subset of \mathbf{R}^2 because the robot is assumed not to rotate in this section.

In the process of the mapping to the C-space \mathcal{Q} , the obstacle \mathcal{O} is inflated, whereas the robot \mathcal{R} is reduced to a point at the origin. The inflated obstacle is called the C-obstacle defined as follows:

Definition 4 (*Configuration space obstacle*) The configuration space obstacle \mathcal{QO} of an obstacle \mathcal{O} to a robot \mathcal{R} is the set of configurations at which the robot \mathcal{R} intersects the obstacle \mathcal{O} , which has the form

$$\mathcal{QO} = \{\mathbf{q} \in \mathcal{Q} | (\{\mathbf{q}\} \oplus \mathcal{F}_{\mathcal{R}}) \cap \mathcal{F}_{\mathcal{O}} \neq \emptyset\}, \quad (2)$$

where \oplus is the Minkowski sum operator defined as

$$\mathcal{A} \oplus \mathcal{B} = \{\mathbf{x} + \mathbf{y} | \mathbf{x} \in \mathcal{A}, \mathbf{y} \in \mathcal{B}\}. \quad (3)$$

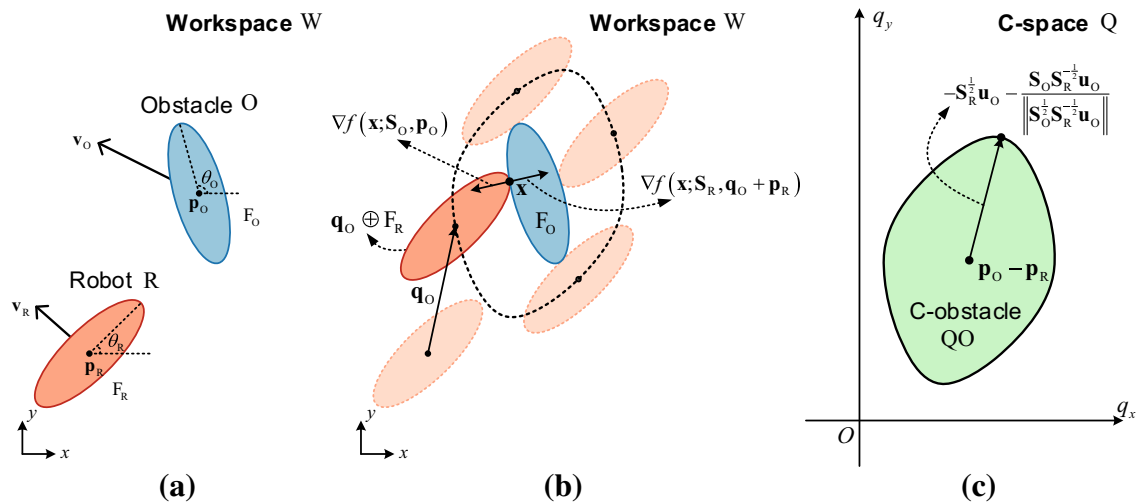


Fig. 2 The construction process of the C-obstacle. **a** A robot \mathcal{R} and an obstacle \mathcal{O} in the workspace \mathcal{W} . **b** A contact point \mathbf{x} between two ellipses, $\{\mathbf{q}_O\} \oplus \mathcal{F}_R$ and \mathcal{F}_O , and the boundary of the C-obstacle $\partial \mathcal{QO}$. **c** The C-obstacle \mathcal{QO} of the obstacle \mathcal{O} with respect to the robot \mathcal{R}

The space represented by \mathcal{QO} is convex because the Minkowski sum preserves convexity of sets. The outline of the C-obstacle \mathcal{QO} is derived as follows.

Lemma 5 Consider a robot \mathcal{R} and an obstacle \mathcal{O} in the planar workspace \mathcal{W} . The boundary of the C-obstacle \mathcal{QO} is the locus of all points that satisfy the equation

$$\mathbf{q}_O = \mathbf{p}_O - \mathbf{p}_R - \mathbf{S}_R^{-\frac{1}{2}} \mathbf{u}_O - \frac{\mathbf{S}_O \mathbf{S}_R^{-\frac{1}{2}} \mathbf{u}_O}{\left\| \mathbf{S}_O \mathbf{S}_R^{-\frac{1}{2}} \mathbf{u}_O \right\|}, \quad (4)$$

where \mathbf{u}_O is a parameter such that $\|\mathbf{u}_O\| = 1$.

Proof From (2), the boundary of the C-obstacle, $\partial \mathcal{QO}$ is a set of points \mathbf{q}_O such that two ellipses $\{\mathbf{q}_O\} \oplus \mathcal{F}_R$ and \mathcal{F}_O touch each other externally, as shown in Fig. 2. Then the tangential point \mathbf{x} satisfies

- (a) $\mathbf{x} \in \partial (\{\mathbf{q}_O\} \oplus \mathcal{F}_R)$;
- (b) $\mathbf{x} \in \partial \mathcal{F}_O$;
- (c) $\nabla f(\mathbf{x}; \mathbf{S}_R, \mathbf{q}_O + \mathbf{p}_R) = -k \nabla f(\mathbf{x}; \mathbf{S}_O, \mathbf{p}_O)$ for some $k > 0$.

From (1), (a) indicates that $\mathbf{x} = \mathbf{q}_O + \mathbf{p}_R + \mathbf{S}_R^{\frac{1}{2}} \mathbf{u}_O$ where $\mathbf{u}_O \in \mathbb{R}^2$ such that $\|\mathbf{u}_O\| = 1$. Similarly, (b) means that $\mathbf{x} = \mathbf{p}_O + \mathbf{S}_O^{\frac{1}{2}} \tilde{\mathbf{u}}_O$ where $\tilde{\mathbf{u}}_O \in \mathbb{R}^2$ such that $\|\tilde{\mathbf{u}}_O\| = 1$. Hence, a point \mathbf{q}_O on $\partial \mathcal{QO}$ is

$$\mathbf{q}_O = \mathbf{p}_O - \mathbf{p}_R - \mathbf{S}_R^{-\frac{1}{2}} \mathbf{u}_O + \mathbf{S}_O^{\frac{1}{2}} \tilde{\mathbf{u}}_O. \quad (5)$$

From (c), for some $k > 0$, $\mathbf{S}_R^{-\frac{1}{2}} \mathbf{u}_O = -k \mathbf{S}_O^{-\frac{1}{2}} \tilde{\mathbf{u}}_O$, which can be written as $\tilde{\mathbf{u}}_O = -\frac{1}{k} \mathbf{S}_O^{\frac{1}{2}} \mathbf{S}_R^{-\frac{1}{2}} \mathbf{u}_O$. Since $\|\tilde{\mathbf{u}}_O\| = 1$,

$$k = \left\| \mathbf{S}_O^{\frac{1}{2}} \mathbf{S}_R^{-\frac{1}{2}} \mathbf{u}_O \right\|. \text{ Hence,}$$

$$\tilde{\mathbf{u}}_O = -\frac{\mathbf{S}_O^{\frac{1}{2}} \mathbf{S}_R^{-\frac{1}{2}} \mathbf{u}_O}{\left\| \mathbf{S}_O^{\frac{1}{2}} \mathbf{S}_R^{-\frac{1}{2}} \mathbf{u}_O \right\|}. \quad (6)$$

Finally, (4) follows from (5) and (6). \square

The first two terms in (4) represent the relative position of the obstacle with respect to the robot, which is the position of the C-obstacle \mathcal{QO} in the C-space \mathcal{Q} , and the last two terms describe its shape parameterized by a unit vector \mathbf{u}_O , as shown in Fig. 2.

3.2 Tangent lines to the configuration space obstacle

In this subsection, tangent lines to the C-obstacle are computed as a preliminary step in deriving the EBVO. Two cases are discussed: when the direction vector of the line is given and when a point on the line is given.

First of all, put $u = [\cos \phi \sin \phi]^T$ in (4). Then we obtain the tangent vector to the C-obstacle \mathcal{QO} at \mathbf{q}_O by taking the derivative of (4) with respect to ϕ :

$$\begin{aligned} \frac{d\mathbf{q}_O}{d\phi} = & -\mathbf{S}_R^{\frac{1}{2}} \mathbf{R}_{\frac{\pi}{2}} \mathbf{u}_O - \frac{1}{k} \mathbf{S}_O \mathbf{S}_R^{-\frac{1}{2}} \mathbf{R}_{\frac{\pi}{2}} \mathbf{u}_O \\ & + \frac{1}{k^3} \left(\mathbf{u}_O^T \mathbf{S}_R^{-\frac{1}{2}} \mathbf{S}_O \mathbf{S}_R^{-\frac{1}{2}} \mathbf{R}_{\frac{\pi}{2}} \mathbf{u}_O \right) \mathbf{S}_O \mathbf{S}_R^{-\frac{1}{2}} \mathbf{u}_O, \end{aligned} \quad (7)$$

where \mathbf{R}_θ is the rotation matrix corresponding to a counter-clockwise rotation of θ .

Lemma 6 Consider the C-obstacle QO whose boundary is represented by (4). If the direction vector of the tangent line to QO is given by \mathbf{d} , then the parameter \mathbf{u}_O^* of the contact point $\mathbf{q}_O^* = \mathbf{p}_O - \mathbf{p}_R - \mathbf{S}_R^{-\frac{1}{2}}\mathbf{u}_O^* - \frac{1}{k}\mathbf{S}_O\mathbf{S}_R^{-\frac{1}{2}}\mathbf{u}_O^*$ satisfies

$$\mathbf{u}_O^{*T}\mathbf{S}_R^{-\frac{1}{2}}\mathbf{d} = 0. \quad (8)$$

Proof At the contact point \mathbf{q}_O^* , it is satisfied that

$$\left. \frac{d\mathbf{q}_O}{d\phi} \right|_{\mathbf{q}_O=\mathbf{q}_O^*} = m\mathbf{d}, \quad (9)$$

where $m \in \mathbb{R} - \{0\}$. Substituting (7) into (9) and left multiplying $\mathbf{u}_O^{*T}\mathbf{S}_R^{-\frac{1}{2}}$ to both sides of (9), we can rewrite the equation as

$$\begin{aligned} & -\mathbf{u}_O^{*T}\mathbf{R}_{\frac{\pi}{2}}\mathbf{u}_O^* - \frac{1}{k}\mathbf{u}_O^{*T}\mathbf{S}_R^{-\frac{1}{2}}\mathbf{S}_O\mathbf{S}_R^{-\frac{1}{2}}\mathbf{R}_{\frac{\pi}{2}}\mathbf{u}_O^* \\ & + \frac{1}{k^3}\left(\mathbf{u}_O^{*T}\mathbf{S}_R^{-\frac{1}{2}}\mathbf{S}_O\mathbf{S}_R^{-\frac{1}{2}}\mathbf{R}_{\frac{\pi}{2}}\mathbf{u}_O^*\right)\left(\mathbf{u}_O^{*T}\mathbf{S}_R^{-\frac{1}{2}}\mathbf{S}_O\mathbf{S}_R^{-\frac{1}{2}}\mathbf{u}_O^*\right) \\ & = m\mathbf{u}_O^{*T}\mathbf{S}_R^{-\frac{1}{2}}\mathbf{d}. \end{aligned} \quad (10)$$

Since $\mathbf{u}_O^{*T}\mathbf{R}_{\frac{\pi}{2}}\mathbf{u}_O^* = 0$ and $k^2 = \mathbf{u}_O^{*T}\mathbf{S}_R^{-\frac{1}{2}}\mathbf{S}_O\mathbf{S}_R^{-\frac{1}{2}}\mathbf{u}_O^*$, the left-hand side of (10) equals to 0. Because $m \neq 0$, we arrive at (8). \square

Lemma 7 Consider the C-obstacle QO whose boundary is represented by (4). The tangent line to QO at point \mathbf{q}_O^* has the form

$$\mathbf{u}_O^{*T}\mathbf{S}_R^{-\frac{1}{2}}(\mathbf{q} - \mathbf{p}_O + \mathbf{p}_R) + \left\| \mathbf{S}_O\mathbf{S}_R^{-\frac{1}{2}}\mathbf{u}_O^* \right\| + 1 = 0, \quad (11)$$

where \mathbf{u}_O^* is the parameter of \mathbf{q}_O^* .

Proof If the direction vector \mathbf{d} is given, the equation of the tangent line has the form $(\mathbf{d}^\perp)^T(\mathbf{q} - \mathbf{q}_O^*) = 0$. Since $\mathbf{d}^\perp = \mathbf{S}_R^{-\frac{1}{2}}\mathbf{u}_O^*$ from (8), (11) holds. \square

From Lemmas 6 and 7, we can derive the equation of the tangent line when its direction vector is given.

Lemma 8 Consider the C-obstacle QO of an elliptic obstacle O to an elliptic robot R . If the direction vector \mathbf{d} of the tangent line is given, the equation of the line can be expressed as

$$\begin{aligned} & \mathbf{d}^T\mathbf{R}_{\frac{\pi}{2}}(\mathbf{q} - \mathbf{p}_O + \mathbf{p}_R) \\ & \pm \left\| \mathbf{S}_O\mathbf{R}_{\frac{\pi}{2}}\mathbf{d} \right\| \pm \sqrt{\det \mathbf{S}_R} \left\| \mathbf{S}_R^{-\frac{1}{2}}\mathbf{d} \right\| = 0. \end{aligned} \quad (12)$$

Proof Suppose that the direction vector \mathbf{d} of the tangent line is given. From Lemma 6, the parameter \mathbf{u}_O^* is given by $\mathbf{u}_O^* = \pm \mathbf{R}_{\frac{\pi}{2}}\mathbf{S}_R^{-\frac{1}{2}}\mathbf{d} / \left\| \mathbf{S}_R^{-\frac{1}{2}}\mathbf{d} \right\|$. Putting \mathbf{u}_O^* into (11) in Lemma 7, we obtain

$$\begin{aligned} & \mathbf{d}^T\mathbf{S}_R^{-\frac{1}{2}}\mathbf{R}_{\frac{\pi}{2}}\mathbf{S}_R^{-\frac{1}{2}}(\mathbf{q} - \mathbf{p}_O + \mathbf{p}_R) \\ & \pm \left\| \mathbf{S}_O\mathbf{S}_R^{-\frac{1}{2}}\mathbf{R}_{\frac{\pi}{2}}\mathbf{S}_R^{-\frac{1}{2}}\mathbf{d} \right\| \pm \left\| \mathbf{S}_R^{-\frac{1}{2}}\mathbf{d} \right\| = 0. \end{aligned} \quad (13)$$

Because $\mathbf{S}_R^{-\frac{1}{2}}\mathbf{R}_{\frac{\pi}{2}}\mathbf{S}_R^{-\frac{1}{2}} = \frac{1}{\sqrt{\det \mathbf{S}_R}}\mathbf{R}_{\frac{\pi}{2}}$ and $\det \mathbf{S}_R > 0$, (13) can be written as (12). \square

Next, suppose that a point \mathbf{q}_0 on the tangent line is given. From Lemma 7, $\mathbf{u}_O^{*T}\mathbf{S}_R^{-\frac{1}{2}}(\mathbf{q}_0 - \mathbf{p}_O + \mathbf{p}_R) + \left\| \mathbf{S}_O\mathbf{S}_R^{-\frac{1}{2}}\mathbf{u}_O^* \right\| + 1 = 0$ is obtained. This equation is transformed into the quadratic form

$$\mathbf{u}_O^{*T}\mathbf{A}\mathbf{u}_O^* + 2\mathbf{u}_O^{*T}\mathbf{b} + 1 = 0 \quad (14)$$

subject to the constraint $\mathbf{u}_O^{*T}\mathbf{b} + 1 < 0$, where $\mathbf{A} = \mathbf{b}\mathbf{b}^T - \mathbf{S}_R^{-\frac{1}{2}}\mathbf{S}_O\mathbf{S}_R^{-\frac{1}{2}}$ and $\mathbf{b} = \mathbf{S}_R^{-\frac{1}{2}}(\mathbf{q}_0 - \mathbf{p}_O + \mathbf{p}_R)$. In order to solve (14), the unit vector \mathbf{u}_O^* is parameterized rationally as $\mathbf{u}_O^* = [1 - t^2 \ 2t]^T / (1 + t^2)$. Then the left-hand side of (14) is written as a fraction whose numerator is $(1 + t^2)^2$ and denominator is

$$\begin{aligned} & (a_{11} - 2b_1 + 1)t^4 + (4b_2 - 4a_{12})t^3 \\ & + (4a_{22} - 2a_{11} + 2)t^2 + (4a_{12} + 4b_2)t \\ & + a_{11} + 2b_1 + 1 = 0, \end{aligned} \quad (15)$$

where a_{ij} is the element of the matrix \mathbf{A} in the i th row and j th column and b_i is the i th element of the vector \mathbf{b} . The equation (15) can be solved as mentioned in Moler (1991): the companion matrix associated with the polynomial is computed, and then the eigenvalues corresponding to the roots of (15) are calculated by the QZ algorithm (Moler and Stewart 1973).

If the degree of the denominator is equal to that of the numerator, which is four, the solution of (14) is equivalent to that of (15). If it is less than four, the solution of (14) involves not only unit vectors associated with the roots of (15) but also $\mathbf{u}_O^* = [-1 \ 0]^T$, which is the limit as $t \rightarrow \infty$. Among the four solutions of (14), only two of them, $\mathbf{u}_{O,1}^*$ and $\mathbf{u}_{O,2}^*$, satisfy $\mathbf{u}_O^{*T}\mathbf{b} + 1 < 0$. Accordingly, the tangent lines containing the given point are represented by, for $i = 1, 2$,

$$\mathbf{u}_{O,i}^{*T}\mathbf{S}_R^{-\frac{1}{2}}(\mathbf{q} - \mathbf{q}_0) = 0. \quad (16)$$

3.3 Construction of ellipse-based velocity obstacles

In this subsection, the EBVO is defined on the basis of the tangent line equations of the C-obstacle derived in the preceding subsection. The VO was defined as the result of the mapping of the C-obstacle to its velocity space in Fiorini and Shiller (1993). When both the robot and the obstacle are ellipses, the VO formed by them is called the *Ellipse-based Velocity Obstacle*.

Definition 9 (*Ellipse-based Velocity Obstacle*) The *ellipse-based velocity obstacle* $VO_{\mathcal{R}|\mathcal{O}}^\tau$ for an elliptic robot \mathcal{R} induced by an elliptic obstacle \mathcal{O} is the set of all the robot's linear velocities \mathbf{v} that would cause a collision with \mathcal{O} within a time horizon $\tau > 0$, given by

$$VO_{\mathcal{R}|\mathcal{O}}^\tau = \left\{ \mathbf{v} \in \mathbb{R}^2 \mid l(\mathbf{0}, \mathbf{v} - \mathbf{v}_{\mathcal{O}}, \tau) \cap \mathcal{QO} \neq \emptyset \right\}, \quad (17)$$

where $l(\mathbf{p}, \mathbf{v}, \tau) = \{\mathbf{p} + t\mathbf{v} \mid 0 \leq t \leq \tau\}$, which is a line segment starting at \mathbf{p} and ending at $\mathbf{p} + \tau\mathbf{v}$.

In Chakravarthy and Ghose (1998), it was proven that a necessary and sufficient condition for the collision between \mathcal{R} and \mathcal{O} was that $\mathbf{v}_{\mathcal{O}} - \mathbf{v}_{\mathcal{R}} \in \text{cone}(\mathcal{QO})$, where $\text{cone}(\mathcal{C})$ was the conic hull of a set \mathcal{C} , given by $\text{cone}(\mathcal{C}) = \left\{ \sum_{i=1}^k \alpha_i \mathbf{q}_i \mid \mathbf{q}_i \in \mathcal{C}, \alpha_i \geq 0 \text{ for all } i, k \in \mathbb{N} \right\}$. From the above condition, the EBVO $VO_{\mathcal{R}|\mathcal{O}}^\infty$ with infinite time horizon can be represented by the translation of the conic hull of the C-obstacle \mathcal{QO} by $\mathbf{v}_{\mathcal{O}}$:

$$VO_{\mathcal{R}|\mathcal{O}}^\infty = \text{cone}(\mathcal{QO}) \oplus \{\mathbf{v}_{\mathcal{O}}\}. \quad (18)$$

As shown in Fig. 3, the region $\text{cone}(\mathcal{QO})$ is bounded by the two tangent lines $l_{\mathcal{O}}^{\text{left}}$ and $l_{\mathcal{O}}^{\text{right}}$. Based on the tangent line equations in Sect. 3.2, the points of tangency can be easily obtained. Let $\mathbf{q}_{\mathcal{O}}^{\text{left}}$ and $\mathbf{q}_{\mathcal{O}}^{\text{right}}$ be the contact points of the lines that pass through the origin and touch the left and right side of \mathcal{QO} , respectively. Also, let $\mathbf{u}_{\mathcal{O}}^{\text{left}}$ and $\mathbf{u}_{\mathcal{O}}^{\text{right}}$ be the parameters of $\mathbf{q}_{\mathcal{O}}^{\text{left}}$ and $\mathbf{q}_{\mathcal{O}}^{\text{right}}$. Then $\text{cone}(\mathcal{QO})$ is the intersection of two half-spaces as the following lemma.

Lemma 10 Suppose $\mathbf{u}_{\mathcal{O}}^{\text{left}}$ and $\mathbf{u}_{\mathcal{O}}^{\text{right}}$ are the parameters of the points $\mathbf{q}_{\mathcal{O}}^{\text{left}}$ and $\mathbf{q}_{\mathcal{O}}^{\text{right}}$ on the lines that pass through the origin and tangent to the C-obstacle \mathcal{QO} . Then the conic hull of \mathcal{QO} , $\text{cone}(\mathcal{QO})$ has the form

$$\text{cone}(\mathcal{QO}) = \left\{ \mathbf{q} \in \mathcal{QO} \mid \mathbf{q}^T \mathbf{S}_{\mathcal{R}}^{-\frac{1}{2}} \mathbf{u}_{\mathcal{O}}^{\text{left}} \geq 0, \mathbf{q}^T \mathbf{S}_{\mathcal{R}}^{-\frac{1}{2}} \mathbf{u}_{\mathcal{O}}^{\text{right}} \geq 0 \right\}. \quad (19)$$

The proof of Lemma 10 is straightforward. Lines $\mathbf{q}^T \mathbf{S}_{\mathcal{R}}^{-\frac{1}{2}} \mathbf{u}_{\mathcal{O}}^{\text{left}} = 0$ and $\mathbf{q}^T \mathbf{S}_{\mathcal{R}}^{-\frac{1}{2}} \mathbf{u}_{\mathcal{O}}^{\text{right}} = 0$ are tangent to \mathcal{QO} from (16).

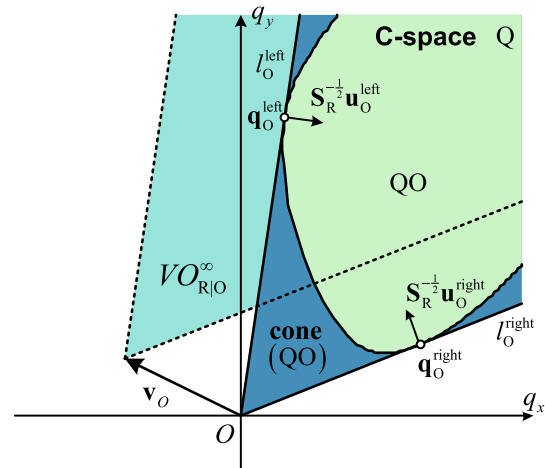


Fig. 3 The conic hull of the C-obstacle \mathcal{QO} , $\text{cone}(\mathcal{QO})$, and the EBVO $VO_{\mathcal{R}|\mathcal{O}}^\infty$. Two tangent lines $l_{\mathcal{O}}^{\text{left}}$ and $l_{\mathcal{O}}^{\text{right}}$ bound the conic hull and touch \mathcal{QO} at $\mathbf{q}_{\mathcal{O}}^{\text{left}}$ and $\mathbf{q}_{\mathcal{O}}^{\text{right}}$, respectively. The normal vectors of the lines are $\mathbf{S}_{\mathcal{R}}^{-\frac{1}{2}} \mathbf{u}_{\mathcal{O}}^{\text{left}}$ and $\mathbf{S}_{\mathcal{R}}^{-\frac{1}{2}} \mathbf{u}_{\mathcal{O}}^{\text{right}}$, where $\mathbf{u}_{\mathcal{O}}^{\text{left}}$ and $\mathbf{u}_{\mathcal{O}}^{\text{right}}$ is the parameters of $\mathbf{q}_{\mathcal{O}}^{\text{left}}$ and $\mathbf{q}_{\mathcal{O}}^{\text{right}}$ in (4). In addition, the EBVO $VO_{\mathcal{R}|\mathcal{O}}^\infty$ is the translation of $\text{cone}(\mathcal{QO})$ by the linear velocity of the obstacle \mathcal{O}

Moreover, $(\mathbf{p}_{\mathcal{O}} - \mathbf{p}_{\mathcal{R}})^T \mathbf{S}_{\mathcal{R}}^{-\frac{1}{2}} \mathbf{u}_{\mathcal{O}}^{\text{left}} = \left\| \mathbf{S}_{\mathcal{O}}^{\frac{1}{2}} \mathbf{S}_{\mathcal{R}}^{-\frac{1}{2}} \mathbf{u}_{\mathcal{O}}^{\text{left}} \right\| + 1 > 0$ and $(\mathbf{p}_{\mathcal{O}} - \mathbf{p}_{\mathcal{R}})^T \mathbf{S}_{\mathcal{R}}^{-\frac{1}{2}} \mathbf{u}_{\mathcal{O}}^{\text{right}} = \left\| \mathbf{S}_{\mathcal{O}}^{\frac{1}{2}} \mathbf{S}_{\mathcal{R}}^{-\frac{1}{2}} \mathbf{u}_{\mathcal{O}}^{\text{right}} \right\| + 1 > 0$ from (11) for $\mathbf{p}_{\mathcal{O}} - \mathbf{p}_{\mathcal{R}} \in \mathcal{QO}$.

Corollary 11 If $\mathbf{u}_{\mathcal{O}}^{\text{left}}$ and $\mathbf{u}_{\mathcal{O}}^{\text{right}}$ are the parameters of the contact points between the lines passing through the origin and the C-obstacle \mathcal{QO} , then $VO_{\mathcal{R}|\mathcal{O}}^\infty$ is expressed as

$$VO_{\mathcal{R}|\mathcal{O}}^\infty = \left\{ \mathbf{v} \in \mathbb{R}^2 \mid (\mathbf{v} - \mathbf{v}_{\mathcal{O}})^T \mathbf{S}_{\mathcal{R}}^{-\frac{1}{2}} \mathbf{u}_{\mathcal{O}}^{\text{left}} \geq 0, (\mathbf{v} - \mathbf{v}_{\mathcal{O}})^T \mathbf{S}_{\mathcal{R}}^{-\frac{1}{2}} \mathbf{u}_{\mathcal{O}}^{\text{right}} \geq 0 \right\}. \quad (20)$$

For a finite value of τ , the cone is truncated by the curve segment $\gamma_{\mathcal{R}|\mathcal{O}}^\tau$, which is a part of the boundary of the shrunk region of \mathcal{QO} by the factor τ :

$$\gamma_{\mathcal{R}|\mathcal{O}}^\tau \subset \left\{ \mathbf{v} \in \mathbb{R}^2 \mid \tau(\mathbf{v} - \mathbf{v}_{\mathcal{O}}) \in \partial \mathcal{QO} \right\}. \quad (21)$$

However, $\gamma_{\mathcal{R}|\mathcal{O}}^\tau$ is not appropriate for the computation of $VO_{\mathcal{R}|\mathcal{O}}^\tau$ because it is difficult to determine whether a point is on the left or right side of the curve.

Hence, we will conservatively approximate $VO_{\mathcal{R}|\mathcal{O}}^\tau$ to $\widetilde{VO}_{\mathcal{R}|\mathcal{O}}^\tau$ by replacing $\gamma_{\mathcal{R}|\mathcal{O}}^\tau$ to its tangent line $\Gamma_{\mathcal{R}|\mathcal{O}}^\tau$, as shown in Fig. 4. The direction vector of $\Gamma_{\mathcal{R}|\mathcal{O}}^\tau$ is designated parallel to $\mathbf{d}_{\mathcal{O}} = \mathbf{q}_{\mathcal{O}}^{\text{left}} - \mathbf{q}_{\mathcal{O}}^{\text{right}}$ to reflect non-symmetry of $\gamma_{\mathcal{R}|\mathcal{O}}^\tau$. In addition, this line is easily obtained from Lemma 8.

preferred linear speed $v_{\mathcal{R}}^{pref}$ and is directed toward $\mathbf{p}_{\mathcal{R}}^{goal}$, as mentioned in Sect. 2:

$$\mathbf{v}_{\mathcal{R}}^{pref} = \frac{v_{\mathcal{R}}^{pref} (\mathbf{p}_{\mathcal{R}}^{goal} - \mathbf{p}_{\mathcal{R}})}{\max \{v_{\mathcal{R}}^{pref} \Delta t, \|\mathbf{p}_{\mathcal{R}}^{goal} - \mathbf{p}_{\mathcal{R}}\|\}}. \quad (27)$$

3.4.4 New linear velocity selection

Problem 2 is generally equivalent to finding the closest velocity to the preferred one in RAV :

$$\mathbf{v}_{\mathcal{R}}^{new} = \arg \min_{\mathbf{v} \in RAV} \|\mathbf{v} - \mathbf{v}_{\mathcal{R}}^{pref}\|. \quad (28)$$

However, solving the problem of (28) is computationally demanding because it has the non-convex domain RAV . Therefore, the ClearPath efficient geometric algorithm introduced in Guy et al. (2009) is employed.

If $\mathbf{v}_{\mathcal{R}}^{pref} \notin \widetilde{VO}_{\mathcal{R}} \setminus \partial \widetilde{VO}_{\mathcal{R}}$, then $\mathbf{v}_{\mathcal{R}}^{pref} \in RAV$ and $\mathbf{v}_{\mathcal{R}}^{new} = \mathbf{v}_{\mathcal{R}}^{pref}$. Otherwise, $\mathbf{v}_{\mathcal{R}}^{new}$ is contained in $\partial \widetilde{VO}_{\mathcal{R}}$. Since $\partial \widetilde{VO}_{\mathcal{R}}$ is the union of line segments, the candidates of $\mathbf{v}_{\mathcal{R}}^{new}$ is classified into three groups:

- VC_A projections of $\mathbf{v}_{\mathcal{R}}^{pref}$ onto the line segments of $\partial \widetilde{VO}_{\mathcal{R}}$,
- VC_B cross velocities between the line segments of $\partial \widetilde{VO}_{\mathcal{R}}$,
- VC_C cross velocities between the boundary of RV and the line segments of $\partial \widetilde{VO}_{\mathcal{R}}$.

Figure 5 presents the combined EBVO $\widetilde{VO}_{\mathcal{R}}$, the region of RAV , and the set of candidates of $\mathbf{v}_{\mathcal{R}}^{new}$, which is $VC = \{VC_A, VC_B, VC_C\}$. The white, gray, and black marks represent VC_A , VC_B , and VC_C , respectively. Among those points, the closest point to $\mathbf{v}_{\mathcal{R}}^{pref}$ is the solution of (28).

However, we further divide the candidates into two parts: VC_h and VC_l . The set VC_h is defined by $VC_h = VC \cap \bigcup_{\mathcal{O}_i \in \mathcal{O}_d} \partial \widetilde{VO}_{\mathcal{R}}|_{\mathcal{O}_i}$, and the set VC_l is defined by $VC_l = VC \setminus VC_h$. If the robot moves with a velocity in VC_h , the robot grazes the obstacles and completely avoid the collisions with them. On the other hand, if the robot moves with a velocity in VC_l , the robot will collide with some of the obstacles after τ . Therefore, we give a high priority to velocities in VC_h when $\mathbf{v}_{\mathcal{R}}^{new}$ is determined. As a result, when $\mathbf{v}_{\mathcal{R}}^{pref} \in \widetilde{VO}_{\mathcal{R}} \setminus \partial \widetilde{VO}_{\mathcal{R}}$, $\mathbf{v}_{\mathcal{R}}^{new}$ is decided as follows:

$$\mathbf{v}_{\mathcal{R}}^{new} = \begin{cases} \arg \min_{\mathbf{v} \in VC_h} \|\mathbf{v} - \mathbf{v}_{\mathcal{R}}^{pref}\|, & \text{if } VC_h \neq \emptyset, \\ \arg \min_{\mathbf{v} \in VC_l} \|\mathbf{v} - \mathbf{v}_{\mathcal{R}}^{pref}\|, & \text{if } VC_h = \emptyset. \end{cases} \quad (29)$$

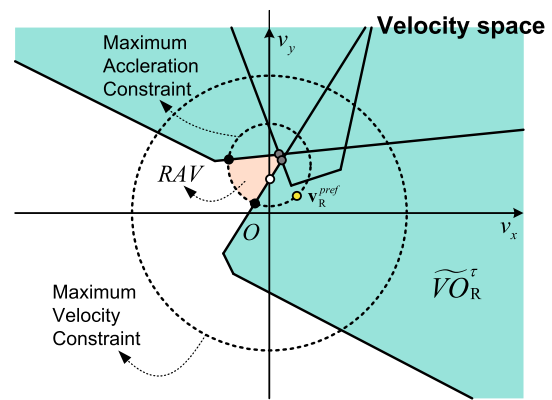


Fig. 5 The selection of the new linear velocity $\mathbf{v}_{\mathcal{R}}^{new}$ in the robot's velocity space. The green region represents $\widetilde{VO}_{\mathcal{R}}$, and the dotted circles indicate the robot's dynamic constraints, and the red region represents RAV . The yellow mark is $\mathbf{v}_{\mathcal{R}}^{pref}$. The white, gray, and black marks are included in the groups VC_A , VC_B , and VC_C , respectively. In this case, the white mark is selected to $\mathbf{v}_{\mathcal{R}}^{new}$ (Color figure online)

If the problem of (28) is infeasible (for example, due to a short sampling period or densely packed conditions), the time horizon τ decreases until the feasible solution is guaranteed.

4 Angular motion control

In this section, we deal with Problem 3, where the angular velocity $w_{\mathcal{R}}^{new}$ is determined when the robot is moving with the linear velocity $\mathbf{v}_{\mathcal{R}}^{new}$ computed in Sect. 3. The objective of the rotation is to change its orientation so that the robot circumvents obstacles with the minimum deviation from the shortest path. If $\mathbf{v}_{\mathcal{R}}^{new} \in RAV \setminus \partial \widetilde{VO}_{\mathcal{R}}$, the rotation is unnecessary because \mathcal{R} already moves toward the goal. Hence, $\mathbf{v}_{\mathcal{R}}^{new} \in \partial \widetilde{VO}_{\mathcal{R}}$ is assumed for the rest of this section.

In fact, the determination of the new linear velocity is highly related with the obstacle it first contacts when it maintains the current velocity for a period of time. Hence, we first estimate the shortest time the robot takes to contact obstacles, and then find the collision-free interval of the robot's rotation angles before the time-to-contact. Next, the preferred angular velocities with which the robot potentially circumvent the obstacle with the minimum possible deviation is calculated. Finally, a strategy for selecting the new angular velocity is presented.

4.1 The shortest time-to-contact

In this subsection, we find the obstacle \mathcal{O}_F that the robot first contacts when it maintains its new velocity $\mathbf{v}_{\mathcal{R}}^{new}$ for a period time. Next, the time T_F it takes to contact \mathcal{O}_F is calculated.

Since it is assumed that $\mathbf{v}_{\mathcal{R}}^{new} \in \partial \widetilde{VO}_{\mathcal{R}}$, $\mathbf{v}_{\mathcal{R}}^{new}$ belongs to one of the three sets VC_A , VC_B , and VC_C . If $\mathbf{v}_{\mathcal{R}}^{new} \in$

$VC_A \cup VC_C$, the robot will contact only one obstacle, which is \mathcal{O}_F . Additionally, if $\mathbf{v}_{\mathcal{R}}^{new} \in \Gamma_{\mathcal{R}|\mathcal{O}_F}$, the time-to-contact is $T_F = \tau$. Otherwise, without loss of generality, suppose the robot pass by the left side of \mathcal{O}_F at a future time, that is $\mathbf{v}_{\mathcal{R}}^{new} \in l_{\mathcal{O}_F}^{left}$. Then T_F is calculated by

$$T_F = \min \left\{ \frac{\|\mathbf{q}_{\mathcal{O}_F}^{left}\|}{\|\mathbf{v}_{\mathcal{R}}^{new} - \mathbf{v}_{\mathcal{O}_F}\|}, \tau \right\}. \quad (30)$$

Because τ is the maximum time for which the collision is considered, T_F is limited below τ .

If $\mathbf{v}_{\mathcal{R}}^{new} \in VC_B$, the robot will contact two obstacles, denoted by $\mathcal{O}_{F,1}$ and $\mathcal{O}_{F,2}$. For each of them, the time-to-contact $T_{F,i}$ is calculated from (30). Afterward, $\mathcal{O}_F = \mathcal{O}_{F,i}$ and $T_F = T_{F,i}$ for $i = \arg \min \{T_{F,1}, T_{F,2}\}$.

4.2 Collision-free rotation angles

With respect to a local frame attached to \mathcal{R} , the robot is rotating at the origin and the obstacle is moving with the velocity $\bar{\mathbf{v}}_{\mathcal{O}} = \mathbf{v}_{\mathcal{O}} - \mathbf{v}_{\mathcal{R}}^{new}$ at $\bar{\mathbf{p}}_{\mathcal{O}} = \mathbf{p}_{\mathcal{O}} - \mathbf{p}_{\mathcal{R}}$ at time t_0 . In this chapter, the homogeneous coordinate is adopted to detect the collision easily when the robot rotates. When an ellipse is located at \mathbf{p} and has the shape matrix \mathbf{S} , its footprint \mathcal{F} can be written as

$$\mathcal{F} = \left\{ \mathbf{x} \mid \begin{bmatrix} \mathbf{x}^T & 1 \end{bmatrix} \mathbf{M} \begin{bmatrix} \mathbf{x}^T & 1 \end{bmatrix}^T \leq 0 \right\}, \quad (31)$$

where \mathbf{M} is a 3×3 symmetric coefficient matrix such that

$$\mathbf{M} = \begin{bmatrix} \mathbf{S}^{-1} & -\mathbf{S}^{-1}\mathbf{p} \\ -\mathbf{p}^T\mathbf{S}^{-1} & \mathbf{p}^T\mathbf{S}^{-1}\mathbf{p} - 1 \end{bmatrix}. \quad (32)$$

As introduced in Choi et al. (2006) and Etayo et al. (2006), the separation condition between two ellipses $\mathcal{F}_{\mathcal{R}}$ and $\mathcal{F}_{\mathcal{O}}$ is associated with the characteristic polynomial, given by

$$\begin{aligned} g(\xi) &= \det(\xi\mathbf{M}_{\mathcal{R}} + \mathbf{M}_{\mathcal{O}}) \\ &= a_3\xi^3 + a_2\xi^2 + a_1\xi + a_0. \end{aligned} \quad (33)$$

Lemma 14 Consider two ellipses $\mathcal{F}_{\mathcal{R}}$ and $\mathcal{F}_{\mathcal{O}}$ that have the coefficient matrices $\mathbf{M}_{\mathcal{R}}$ and $\mathbf{M}_{\mathcal{O}}$, respectively. If the characteristic polynomial $g(\xi)$ has two distinct positive real roots and a negative real root, the two ellipses are separated by a line, and vice versa.

Lemma 15 The third-order polynomial $g(\xi) = a_3\xi^3 + a_2\xi^2 + a_1\xi + a_0$ has two distinct positive real roots and a negative real root if and only if

$$\begin{aligned} (a) \quad & -3a_3a_1 + a_2^2 > 0, \\ (b) \quad & -27a_3^2a_0^2 + 18a_3a_2a_1a_0 + a_2^2a_1^2 - 4a_2^3a_0 - 4a_3a_1^3 > 0, \end{aligned}$$

$$(c) \quad a_2a_3 < 0 \text{ or } 3a_3^2a_2a_0 + a_3a_2^2a_1 - 4a_3^2a_1^2 < 0.$$

The proofs of Lemmas 14 and 15 are included in Choi et al. (2006) and Etayo et al. (2006), respectively.

From these lemmas, the collision-free interval of the rotation angles is calculated. As a preliminary step, we first investigate a fixed elliptic obstacle and a fixed line segment obstacle. Afterward, the collision-free interval induced by a moving elliptic obstacle is calculated based on these results.

4.2.1 Fixed elliptic obstacle

Suppose that there are a rotating elliptic robot \mathcal{R} at the origin and an elliptic obstacle fixed at $\bar{\mathbf{p}}_{\mathcal{O}}$, which are initially separated each other. Let $\Delta\theta_{\mathcal{R}}$ be the rotation angle of the robot. The coefficient matrices of the robot and the obstacle are respectively represented by

$$\mathbf{M}_{\mathcal{R}}(t) = \begin{bmatrix} \mathbf{R}_{\Delta\theta_{\mathcal{R}}} \mathbf{S}_{\mathcal{R}}^{-1} \mathbf{R}_{\Delta\theta_{\mathcal{R}}}^T & \mathbf{0} \\ \mathbf{0} & -1 \end{bmatrix}, \quad (34)$$

$$\mathbf{M}_{\mathcal{O}} = \begin{bmatrix} \mathbf{S}_{\mathcal{O}}^{-1} & -\mathbf{S}_{\mathcal{O}}^{-1}\bar{\mathbf{p}}_{\mathcal{O}} \\ -\bar{\mathbf{p}}_{\mathcal{O}}^T\mathbf{S}_{\mathcal{O}}^{-1} & \bar{\mathbf{p}}_{\mathcal{O}}^T\mathbf{S}_{\mathcal{O}}^{-1}\bar{\mathbf{p}}_{\mathcal{O}} - 1 \end{bmatrix}. \quad (35)$$

Then the characteristic polynomial of (33) has the coefficients

$$a_3 = -\det \mathbf{S}_{\mathcal{R}}^{-1}, \quad (36)$$

$$a_2 = a_{22} + a_{21} \cos 2\Delta\theta_{\mathcal{R}} + a_{20} \sin 2\Delta\theta_{\mathcal{R}}, \quad (37)$$

$$a_1 = a_{12} + a_{11} \cos 2\Delta\theta_{\mathcal{R}} + a_{10} \sin 2\Delta\theta_{\mathcal{R}}, \quad (38)$$

$$a_0 = -\det \mathbf{S}_{\mathcal{O}}^{-1}, \quad (39)$$

where

$$a_{22} = (\bar{\mathbf{p}}_{\mathcal{O}}^T \mathbf{S}_{\mathcal{O}}^{-1} \bar{\mathbf{p}}_{\mathcal{O}} - 1) \det \mathbf{S}_{\mathcal{R}}^{-1} - \frac{1}{2} \text{tr} \mathbf{S}_{\mathcal{R}}^{-1} \text{tr} \mathbf{S}_{\mathcal{O}}^{-1}, \quad (40)$$

$$a_{21} = \text{tr} (\mathbf{S}_{\mathcal{R}}^{-1} \mathbf{S}_{\mathcal{O}}^{-1}) - \frac{1}{2} \text{tr} \mathbf{S}_{\mathcal{R}}^{-1} \text{tr} \mathbf{S}_{\mathcal{O}}^{-1}, \quad (41)$$

$$a_{20} = \text{tr} (\mathbf{R}_{\frac{\pi}{2}} \mathbf{S}_{\mathcal{R}}^{-1} \mathbf{S}_{\mathcal{O}}^{-1}), \quad (42)$$

$$a_{12} = \frac{1}{2} \text{tr} \mathbf{S}_{\mathcal{R}}^{-1} (\bar{\mathbf{p}}_{\mathcal{O}}^T \bar{\mathbf{p}}_{\mathcal{O}} \det \mathbf{S}_{\mathcal{O}}^{-1} - \text{tr} \mathbf{S}_{\mathcal{O}}^{-1}) - \det \mathbf{S}_{\mathcal{O}}^{-1}, \quad (43)$$

$$\begin{aligned} a_{11} &= \bar{\mathbf{p}}_{\mathcal{O}}^T (\mathbf{S}_{\mathcal{R}}^{-1} - \frac{1}{2} \mathbf{I}_2 \text{tr} \mathbf{S}_{\mathcal{R}}^{-1}) \bar{\mathbf{p}}_{\mathcal{O}} \det \mathbf{S}_{\mathcal{O}}^{-1} \\ &\quad + \text{tr} (\mathbf{S}_{\mathcal{R}}^{-1} \mathbf{S}_{\mathcal{O}}^{-1}) - \frac{1}{2} \text{tr} \mathbf{S}_{\mathcal{R}}^{-1} \text{tr} \mathbf{S}_{\mathcal{O}}^{-1} \end{aligned} \quad (44)$$

$$a_{10} = \bar{\mathbf{p}}_{\mathcal{O}}^T \mathbf{R}_{\frac{\pi}{2}} \left(\mathbf{S}_{\mathcal{R}}^{-1} - \frac{1}{2} \mathbf{I}_2 \text{tr} \mathbf{S}_{\mathcal{R}}^{-1} \right) \bar{\mathbf{p}}_{\mathcal{O}} \det \mathbf{S}_{\mathcal{O}}^{-1} + \text{tr} \left(\mathbf{R}_{\frac{\pi}{2}} \mathbf{S}_{\mathcal{R}}^{-1} \mathbf{S}_{\mathcal{O}}^{-1} \right). \quad (45)$$

If we substitute (36)–(45) into the inequalities in Lemma 15 and put $\cos 2\Delta\theta_{\mathcal{R}} = (1 - \zeta^2) / (1 + \zeta^2)$ and $\sin 2\Delta\theta_{\mathcal{R}} = 2\zeta / (1 + \zeta^2)$, the polynomial inequalities of degree 4, 8, 2, and 6 are obtained in regular sequence. These inequalities can be solved by finding the roots of the polynomials, and how to solve them is described in Sect. 3.2. As a result, we can derive the collision-free interval of ζ that guarantees the polynomial of (33) has two distinct positive real roots and a negative real root by intersecting the three intervals in Lemma 15.

Afterward, the collision free rotation angles of \mathcal{R} induced by \mathcal{O} , $FA_{\mathcal{R}|\mathcal{O}} = [\Delta\theta_{\mathcal{R}|\mathcal{O}}^{\min}, \Delta\theta_{\mathcal{R}|\mathcal{O}}^{\max}]$ is calculated from that of ζ .

4.2.2 Fixed line segment obstacle

Suppose there are a rotating elliptic robot \mathcal{R} at the origin and a line segment obstacle \mathcal{O} whose end points are $\bar{\mathbf{p}}_{\mathcal{O}}$ and $\bar{\mathbf{p}}_{\mathcal{O}} + T_F \bar{\mathbf{v}}_{\mathcal{O}}$, which are initially separated each other. The distance between the line segment and the origin is given by

$$d_{\mathcal{O}} = \|\bar{\mathbf{p}}_{\mathcal{O}} + \gamma \bar{\mathbf{v}}_{\mathcal{O}}\|, \quad (46)$$

where

$$\gamma = \begin{cases} T_F & \text{if } \bar{\mathbf{p}}_{\mathcal{O}}^T \bar{\mathbf{v}}_{\mathcal{O}} \leq -T_F \bar{\mathbf{v}}_{\mathcal{O}}^T \bar{\mathbf{v}}_{\mathcal{O}}, \\ -\frac{\bar{\mathbf{p}}_{\mathcal{O}}^T \bar{\mathbf{v}}_{\mathcal{O}}}{\bar{\mathbf{v}}_{\mathcal{O}}^T \bar{\mathbf{v}}_{\mathcal{O}}} & \text{if } -T_F \bar{\mathbf{v}}_{\mathcal{O}}^T \bar{\mathbf{v}}_{\mathcal{O}} < \bar{\mathbf{p}}_{\mathcal{O}}^T \bar{\mathbf{v}}_{\mathcal{O}} \leq 0, \\ 0 & \text{if } \bar{\mathbf{p}}_{\mathcal{O}}^T \bar{\mathbf{v}}_{\mathcal{O}} > 0. \end{cases} \quad (47)$$

If $d_{\mathcal{O}} \geq \sqrt{\lambda_{\max}(\mathbf{S}_{\mathcal{R}})}$, the robot is free of collision and $FA_{\mathcal{R}|\mathcal{O}} = [-\pi, \pi]$. Otherwise, the calculation of $FA_{\mathcal{R}|\mathcal{O}}$ is decomposed into three steps.

First of all, it is tested whether the rotating robot will touch the line segment. To this end, the line containing the segment is considered, which is $d_{\text{line}} = \|\bar{\mathbf{p}}_{\mathcal{O}} - (\bar{\mathbf{p}}_{\mathcal{O}}^T \bar{\mathbf{v}}_{\mathcal{O}} / \bar{\mathbf{v}}_{\mathcal{O}}^T \bar{\mathbf{v}}_{\mathcal{O}}) \bar{\mathbf{v}}_{\mathcal{O}}\|$ away from the origin.

Lemma 16 Consider a rotating ellipse \mathcal{R} at the origin and a line d_{line} far from the origin. Then the point $\mathbf{x} \in \partial\mathcal{F}_{\mathcal{R}}$ will contact the line if

$$\mathbf{x}^T \mathbf{S}_{\mathcal{R}}^{-2} \mathbf{x} = \frac{1}{d_{\text{line}}^2}. \quad (48)$$

Proof For $\mathbf{x} \in \partial\mathcal{F}_{\mathcal{R}}$, $f(\mathbf{x}; \mathbf{S}_{\mathcal{R}}, \mathbf{0}) = \mathbf{x}^T \mathbf{S}_{\mathcal{R}}^{-1} \mathbf{x} - 1 = 0$ holds. Suppose the ellipse touches the line when it rotates by θ . Then $\mathbf{x}^* = \mathbf{R}_{\theta} \mathbf{x}$ is on the line and its normal vector $\mathbf{n}^* = \mathbf{R}_{\theta} \mathbf{S}_{\mathcal{R}}^{-1} \mathbf{x}$ is perpendicular to the line, which implies $\mathbf{x}^{*T} \mathbf{n}^* / \|\mathbf{n}^*\| = d_{\text{line}}$. Hence (48) follows. \square

Since $\mathbf{x} = \mathbf{S}_{\mathcal{R}}^{\frac{1}{2}} \mathbf{u}$ can be parameterized by a unit vector \mathbf{u} , (48) can be written as $\mathbf{u}^T \mathbf{S}_{\mathcal{R}}^{-1} \mathbf{u} = 1/d_{\text{line}}^2$. This can be solved by putting $\mathbf{u} = [1 - t^2 \ 2t]^T / (1 + t^2)$. As a result, we obtain the four candidate points $\mathbf{x}_i = \mathbf{S}_{\mathcal{R}}^{\frac{1}{2}} \mathbf{u}_i$ and corresponding normal vectors $\mathbf{n}_i = \mathbf{S}_{\mathcal{R}}^{-\frac{1}{2}} \mathbf{u}_i$ for $i = 1, \dots, 4$. Hence, the robot touches the line when it rotates by angles of $\Delta\theta_{\mathcal{R}}$ such that, for $\mu > 0$,

$$\bar{\mathbf{p}}_{\mathcal{O}} - \frac{\bar{\mathbf{p}}_{\mathcal{O}}^T \bar{\mathbf{v}}_{\mathcal{O}}}{\bar{\mathbf{v}}_{\mathcal{O}}^T \bar{\mathbf{v}}_{\mathcal{O}}} \bar{\mathbf{v}}_{\mathcal{O}} = \mu \mathbf{R}_{\Delta\theta_{\mathcal{R}}}^T \mathbf{n}_i. \quad (49)$$

From (49), we obtain $\Delta\theta_{\mathcal{R},i} \in [-\pi, \pi]$ for $i = 1, \dots, 4$. The collision-free interval of the angular displacements has the form $[\Delta\theta_{\mathcal{R},l}, \Delta\theta_{\mathcal{R},r}]$ from the maximum negative $\Delta\theta_{\mathcal{R},l}$ and the minimum positive $\Delta\theta_{\mathcal{R},r}$. However, if $\mathbf{R}_{\Delta\theta_{\mathcal{R},l}} \mathbf{x}_l$ or $\mathbf{R}_{\Delta\theta_{\mathcal{R},r}} \mathbf{x}_r$ is not on the line segment, the corresponding result is neglected.

Next, the collision-free intervals induced by the two end-points are calculated. For $\bar{\mathbf{p}}_{\mathcal{O}}$, it follows that $\|\mathbf{x}\| = \|\bar{\mathbf{p}}_{\mathcal{O}}\|$.

Writing $\mathbf{x} = \mathbf{S}_{\mathcal{R}}^{\frac{1}{2}} \mathbf{u}$, $\mathbf{u}^T \mathbf{S}_{\mathcal{R}} \mathbf{u} = \bar{\mathbf{p}}_{\mathcal{O}}^T \bar{\mathbf{p}}_{\mathcal{O}}$. This can be solved in the similar way as before, and we can obtain the interval induced by the point $\bar{\mathbf{p}}_{\mathcal{O}}$. Likewise, we can get the interval induced by the point $\bar{\mathbf{p}}_{\mathcal{O}} + T_F \bar{\mathbf{v}}_{\mathcal{O}}$.

Finally, $FA_{\mathcal{R}|\mathcal{O}}$, the collision-free interval induced by \mathcal{O} , is computed by intersecting the above intervals.

4.2.3 Moving elliptic obstacle

Suppose that there are a rotating elliptic robot \mathcal{R} at the origin and an elliptic obstacle \mathcal{O} moving with the velocity $\bar{\mathbf{v}}_{\mathcal{O}}$ at $\bar{\mathbf{p}}_{\mathcal{O}}$ at time t_0 . Let $\mathcal{T}_{\mathcal{O}}$ denote the region swept by the obstacle \mathcal{O} for $[t_0, t_0 + T_F]$ such that

$$\mathcal{T}_{\mathcal{O}} = \bigcup_{t \in [0, T_F]} \{\mathbf{x} \mid f(\mathbf{x}; \mathbf{S}_{\mathcal{O}}, \bar{\mathbf{v}}_{\mathcal{O}} t + \bar{\mathbf{p}}_{\mathcal{O}}) \leq 0\}. \quad (50)$$

As shown in Fig. 6, its boundary $\partial\mathcal{T}_{\mathcal{O}}$ consists of segments of two ellipses and two lines. More specifically, the two ellipses are $\mathcal{T}_{\mathcal{O},1} = \{\mathbf{x} \mid f(\mathbf{x}; \mathbf{S}_{\mathcal{O}}, \bar{\mathbf{p}}_{\mathcal{O}}) \leq 0\}$ and $\mathcal{T}_{\mathcal{O},2} = \{\mathbf{x} \mid f(\mathbf{x}; \mathbf{S}_{\mathcal{O}}, \bar{\mathbf{p}}_{\mathcal{O}} + T_F \bar{\mathbf{v}}_{\mathcal{O}}) \leq 0\}$, and the two line segments are $\mathcal{T}_{\mathcal{O},i} = l(\mathbf{p}_{T,i}, \bar{\mathbf{v}}_{\mathcal{O}}, T_F)$ where $\mathbf{p}_{T,i} = \bar{\mathbf{p}}_{\mathcal{O}} \pm \mathbf{S}_{\mathcal{O}} \bar{\mathbf{v}}_{\mathcal{O}} / (\bar{\mathbf{v}}_{\mathcal{O}}^T \mathbf{S}_{\mathcal{O}} \bar{\mathbf{p}}_{\mathcal{O}})$ for $i = 3, 4$.

The collision-free intervals of the angular displacements induced by $\mathcal{T}_{\mathcal{O},i}$ for $i = 1, 2$, denoted by $FA_{\mathcal{R}|\mathcal{T}_{\mathcal{O},i}}$, can be obtained by the method explained in Sect. 4.2.1. In addition, the intervals induced by $\mathcal{T}_{\mathcal{O},i}$ for $i = 3, 4$, $FA_{\mathcal{R}|\mathcal{T}_{\mathcal{O},i}}$, can be derived as mentioned in Sect. 4.2.2. Finally, the collision-free angular displacements induced by \mathcal{O} is computed by

$$FA_{\mathcal{R}|\mathcal{O}} = \bigcap_{i \in \{1, \dots, 4\}} FA_{\mathcal{R}|\mathcal{T}_{\mathcal{O},i}}. \quad (51)$$

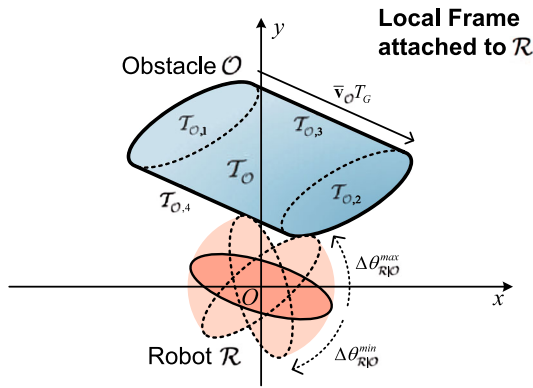


Fig. 6 The collision-free angular displacements of the robot \mathcal{R} in time interval $[0, T_F]$. The swept region by \mathcal{O} for $[t_0, t_0 + T_F]$ is represented by the region $\mathcal{T}_{\mathcal{O}}$. The obstacle \mathcal{O} is $\mathcal{T}_{\mathcal{O},1}$ at time t_0 and $\mathcal{T}_{\mathcal{O},2}$ at time $t_0 + T_F$. The line segments $\mathcal{T}_{\mathcal{O},3}$ and $\mathcal{T}_{\mathcal{O},4}$ are the boundary lines of $\mathcal{T}_{\mathcal{O}}$. The red region indicates the collision-free angular displacements (Color figure online)

In conclusion, we write the following theorem.

Theorem 17 Consider an elliptic robot \mathcal{R} moving with $\mathbf{v}_{\mathcal{R}}^{new}$ at $\mathbf{p}_{\mathcal{R}}$ and an elliptic obstacle \mathcal{O} moving with $\mathbf{v}_{\mathcal{O}}$ at $\mathbf{p}_{\mathcal{O}}$. The robot \mathcal{R} do not collide with the obstacle \mathcal{O} if the robot rotates by an angle of $\Delta\theta_{\mathcal{R}} \in FA_{\mathcal{R}|\mathcal{O}}$, which is calculated as mentioned in Sect. 4.2.3 by setting $\bar{\mathbf{v}}_{\mathcal{O}} = \mathbf{v}_{\mathcal{O}} - \mathbf{v}_{\mathcal{R}}^{new}$ and $\bar{\mathbf{p}}_{\mathcal{O}} = \mathbf{p}_{\mathcal{O}} - \mathbf{p}_{\mathcal{R}}$.

4.3 Preferred angular velocities

As mentioned in Sect. 2, the preferred angular velocities $w_{\mathcal{R},i}^{pref}$ are determined to lead the robot to potentially circumvent obstacles with the minimum possible deviation. Due to symmetry of an ellipse, there are two preferred angular velocities: one is positive and the other is negative.

In this subsection, we start with the following lemma concerning about the C-obstacle with respect to a holonomic robot. Because the parameter $\tilde{\mathbf{u}}_{\mathcal{O}}$ is used to describe the boundary of an obstacle in Sect. 3, it is invariant to the rotation of the robot. That is why the following lemmas and theorem is described with respect to $\tilde{\mathbf{u}}_{\mathcal{O}}$ instead of $\mathbf{u}_{\mathcal{O}}$ unlike the preceding chapter.

Lemma 18 Consider a holonomic elliptic robot \mathcal{R} and an elliptic obstacle \mathcal{O} in the planar workspace \mathcal{W} . If the robot rotates by an angle of ϕ , the boundary of the C-obstacle $\mathcal{QO}(\phi)$ has the form

$$\mathbf{q}_{\mathcal{O}}(\phi) = \mathbf{p}_{\mathcal{O}} - \mathbf{p}_{\mathcal{R}} - \mathbf{S}_{\mathcal{O}}^{\frac{1}{2}} \tilde{\mathbf{u}}_{\mathcal{O}} - \frac{\mathbf{R}_{\phi} \mathbf{S}_{\mathcal{R}} \mathbf{R}_{\phi}^T \mathbf{S}_{\mathcal{O}}^{-\frac{1}{2}} \tilde{\mathbf{u}}_{\mathcal{O}}}{\left\| \mathbf{S}_{\mathcal{R}}^{\frac{1}{2}} \mathbf{R}_{\phi}^T \mathbf{S}_{\mathcal{O}}^{-\frac{1}{2}} \tilde{\mathbf{u}}_{\mathcal{O}} \right\|}, \quad (52)$$

where $\tilde{\mathbf{u}}_{\mathcal{O}}$ is a parameter such that $\|\tilde{\mathbf{u}}_{\mathcal{O}}\| = 1$.

The proof follows from Lemma 5. From Lemmas 7 and 18, we can derive the tangent line to the C-obstacle given rotation angle ϕ .

Lemma 19 Consider the C-obstacle $\mathcal{QO}(\phi)$ with the boundary represented by (52). The tangent line at a point $\mathbf{q}_{\mathcal{O}}^*(\phi) \in \partial \mathcal{QO}(\phi)$ has the form

$$\tilde{\mathbf{u}}_{\mathcal{O}}^{*T} \mathbf{S}_{\mathcal{O}}^{-\frac{1}{2}} (\mathbf{q} - \mathbf{p}_{\mathcal{O}} + \mathbf{p}_{\mathcal{R}}) + \left\| \mathbf{S}_{\mathcal{R}}^{\frac{1}{2}} \mathbf{R}_{\phi} \mathbf{S}_{\mathcal{O}}^{-\frac{1}{2}} \tilde{\mathbf{u}}_{\mathcal{O}}^* \right\| + 1 = 0, \quad (53)$$

where $\tilde{\mathbf{u}}_{\mathcal{O}}^*$ is the parameter of $\mathbf{q}_{\mathcal{O}}^*(\phi)$.

Lemma 20 Consider the C-obstacle $\mathcal{QO}(\phi)$ with the boundary represented by (52). Then

$$\min_{\phi} (D(\tilde{\mathbf{u}}_{\mathcal{O}}^*, \phi)) = \sqrt{\lambda_{\min}(\mathbf{S}_{\mathcal{R}})} + \frac{1}{\left\| \mathbf{S}_{\mathcal{O}}^{-\frac{1}{2}} \tilde{\mathbf{u}}_{\mathcal{O}}^* \right\|}, \quad (54)$$

where $D(\tilde{\mathbf{u}}_{\mathcal{O}}^*, \phi)$ is the distance from the position of the C-obstacle, $\mathbf{p}_{\mathcal{O}} - \mathbf{p}_{\mathcal{R}}$, to its tangent line perpendicular to $\mathbf{S}_{\mathcal{O}}^{-\frac{1}{2}} \tilde{\mathbf{u}}_{\mathcal{O}}^*$.

Proof From Lemma 6, a normal vector at $\mathbf{q}_{\mathcal{O}}^*(\phi) \in \partial \mathcal{QO}(\phi)$ is $\mathbf{S}_{\mathcal{O}}^{-\frac{1}{2}} \tilde{\mathbf{u}}_{\mathcal{O}}^*$. Then the distance is expressed as

$$D(\tilde{\mathbf{u}}_{\mathcal{O}}^*, \phi) = \frac{\left| \tilde{\mathbf{u}}_{\mathcal{O}}^{*T} \mathbf{S}_{\mathcal{O}}^{-\frac{1}{2}} (\mathbf{q} - \mathbf{p}_{\mathcal{O}} + \mathbf{p}_{\mathcal{R}}) \right|}{\left\| \mathbf{S}_{\mathcal{O}}^{-\frac{1}{2}} \tilde{\mathbf{u}}_{\mathcal{O}}^* \right\|}. \quad (55)$$

From (53) and the equality $\left\| \mathbf{S}_{\mathcal{O}}^{-\frac{1}{2}} \tilde{\mathbf{u}}_{\mathcal{O}}^* \right\| = \left\| \mathbf{R}_{\phi} \mathbf{S}_{\mathcal{O}}^{-\frac{1}{2}} \tilde{\mathbf{u}}_{\mathcal{O}}^* \right\|$,

$$D(\tilde{\mathbf{u}}_{\mathcal{O}}^*, \phi) = \frac{\left\| \mathbf{S}_{\mathcal{R}}^{\frac{1}{2}} \mathbf{R}_{\phi} \mathbf{S}_{\mathcal{O}}^{-\frac{1}{2}} \tilde{\mathbf{u}}_{\mathcal{O}}^* \right\|}{\left\| \mathbf{R}_{\phi} \mathbf{S}_{\mathcal{O}}^{-\frac{1}{2}} \tilde{\mathbf{u}}_{\mathcal{O}}^* \right\|} + \frac{1}{\left\| \mathbf{S}_{\mathcal{O}}^{-\frac{1}{2}} \tilde{\mathbf{u}}_{\mathcal{O}}^* \right\|}. \quad (56)$$

Because $\min_{\mathbf{x} \neq 0} \left\| \mathbf{S}_{\mathcal{R}}^{\frac{1}{2}} \mathbf{x} \right\| / \|\mathbf{x}\| = \sqrt{\lambda_{\min}(\mathbf{S}_{\mathcal{R}})}$, we arrive at (54). \square

From Lemma 20, we write the following theorem and corollary.

Theorem 21 Consider a holonomic elliptic robot \mathcal{R} and an elliptic obstacle \mathcal{O} moving with $\mathbf{v}_{\mathcal{O}}$ in the planar workspace \mathcal{W} . If the robot is moving to the direction perpendicular to $\mathbf{S}_{\mathcal{O}}^{-\frac{1}{2}} \tilde{\mathbf{u}}_{\mathcal{O}}$, the robot can maintain its direction without collision by rotating its orientation if and only if

$$\tilde{\mathbf{u}}_{\mathcal{O}}^{*T} \mathbf{S}_{\mathcal{O}}^{-\frac{1}{2}} (\mathbf{q} - \mathbf{p}_{\mathcal{O}} + \mathbf{p}_{\mathcal{R}}) + \left\| \mathbf{S}_{\mathcal{O}}^{-\frac{1}{2}} \tilde{\mathbf{u}}_{\mathcal{O}}^* \right\| \sqrt{\lambda_{\min}(\mathbf{S}_{\mathcal{R}})} + 1 < 0. \quad (57)$$

Corollary 22 *The collision condition between a holonomic elliptic robot \mathcal{R} and an elliptic obstacle \mathcal{O} moving with $\mathbf{v}_{\mathcal{O}}$ is equivalent to that of an circular robot with radius of $\sqrt{\lambda_{\min}(\mathbf{S}_{\mathcal{R}})}$ and the obstacle \mathcal{O} .*

From Theorem 21 and Corollary 22, we know that the robot \mathcal{R} with rotation can circumvent an obstacle as if it is a circular robot with radius equal to its minor radius. Therefore, we first construct the approximated EBVO $\widehat{VO}_{\mathcal{R}_C|\mathcal{O}_F}^{\tau}$ for the circular robot \mathcal{R}_C with radius of $\sqrt{\lambda_{\min}(\mathbf{S}_{\mathcal{R}})}$ induced by the obstacle \mathcal{O}_F that the robot first contacts.

If $\mathbf{v}_{\mathcal{R}}^{pref} \in \widehat{VO}_{\mathcal{R}_C|\mathcal{O}_F}^{\tau}$, the closest velocity \mathbf{v} to $\mathbf{v}_{\mathcal{R}}^{pref}$ is selected outside $\widehat{VO}_{\mathcal{R}_C|\mathcal{O}_F}^{\tau}$. Then the preferred angular orientations are aligned with the direction of $\mathbf{v} - \mathbf{v}_{\mathcal{O}}$. If $\mathbf{v}_{\mathcal{R}}^{pref} \notin \widehat{VO}_{\mathcal{R}_C|\mathcal{O}_F}^{\tau}$, the distance between the robot's path and the obstacle \mathcal{O}_F is calculated. Next, the preferred angular orientations are calculated from Lemma 16. Among the four angles, the minimum positive and the maximum negative ones are assigned to the preferred angular orientations.

4.4 New angular velocity selection

From the collision-free interval of the angular velocities in Sect. 4.2 and the preferred angular velocities in Sect. 4.3, the new angular velocity is determined.

4.4.1 Combined collision-free angular velocities

Similar to Sect. 3.4.1, \mathcal{O}_d is defined as the set of obstacles detected by \mathcal{R} . For $\mathcal{O}_i \in \mathcal{O}_d$, $FA_{\mathcal{R}|\mathcal{O}_i}$ is derived from the method in Sect. 4.2.1. Hence, the combined collision-free interval is

$$FA_{\mathcal{R}} = \bigcap_{\mathcal{O}_i \in \mathcal{O}_d} FA_{\mathcal{R}|\mathcal{O}_i}. \quad (58)$$

The collision-free interval of the robot's angular velocities is calculated by dividing that of the rotation angles with the sampling time Δt :

$$FW_{\mathcal{R}} = \{w \mid w\Delta t \in FA_{\mathcal{R}}\}. \quad (59)$$

If the robot moves with the velocity $\mathbf{v}_{\mathcal{R}}^{new}$ and rotates with angular velocities inside of $FW_{\mathcal{R}}$, the robot do not collide with the obstacles within Δt .

4.4.2 Reachable avoidance angular velocities

The available angular velocities during the next period are limited as the set of reachable angular velocities

$$RW = \{w \mid |w| \leq w_{\mathcal{R}}^{max}, |w - w_{\mathcal{R}}| \leq \alpha_{\mathcal{R}}^{max} \Delta t\}. \quad (60)$$

By intersecting $FW_{\mathcal{R}}$ and RW , the set of reachable avoidance angular velocities is denoted as

$$RAW = FW_{\mathcal{R}} \cap RW. \quad (61)$$

Thus, the robot should select $w_{\mathcal{R}}^{new}$ in RAW .

4.4.3 New angular velocity selection

Problem 3 is equivalent to finding the closest to $w_{\mathcal{R}}^{pref}$ in RAW :

$$w_{\mathcal{R}}^{new} = \arg \min_{w \in RAW} \min_{i=1,2} |\mathbf{w} - \mathbf{w}_{\mathcal{R},i}^{pref}|. \quad (62)$$

If both of the preferred angular velocities are in RAW , the closest to the current angular velocity is selected.

5 Simulation results

The proposed algorithm was implemented and tested in three scenarios. For each of them, the following three algorithms were compared.

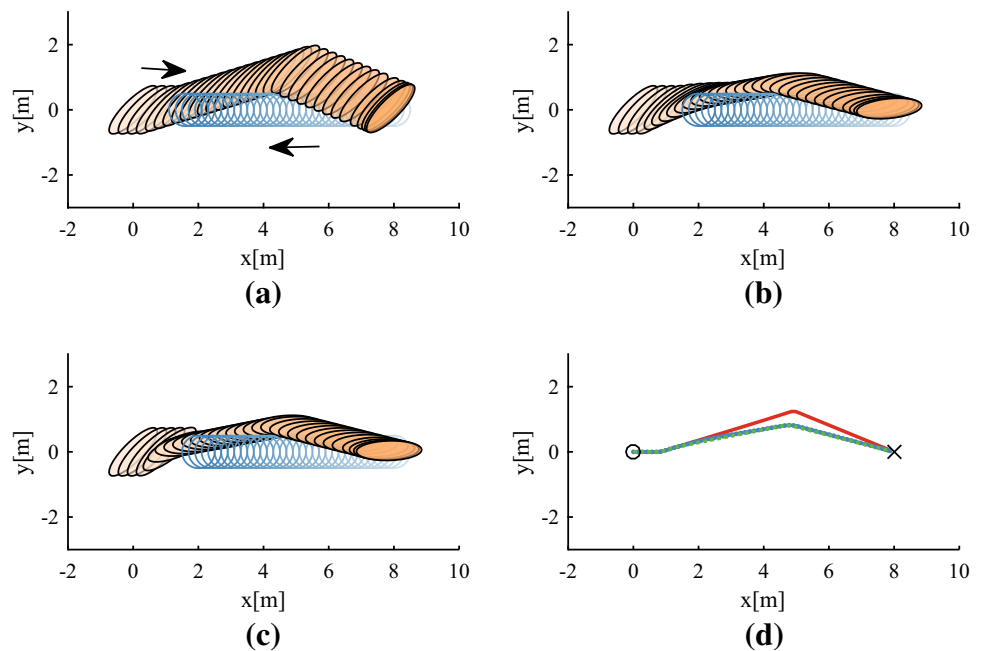
- (a) No Rotation: the robot motion consists only of translation.
- (b) Jeon and Lee (2014): the angular velocity is determined proportional to the change rate of the boundary line of the EBVO with respect to its orientation.
- (c) The proposed algorithm: the angular velocity is determined with which the robot can circumvent obstacles with the minimum deviation.

5.1 Implementation details

The algorithm was implemented in Visual Studio C++ on a PC equipped with Intel Core i7-3770 3.40GHz CPU. In the simulations, the robot's parameters were assigned as follows. The robot was an ellipse whose major and minor radii were 1 m and 0.3 m. Also, the robot detected obstacles in the range of $\rho = 10$ m with a sampling period $\Delta t = 0.2$ s and avoided them by considering the collisions within $\tau = 5$ s. In addition, the preferred linear speed was $v_{\mathcal{R}}^{pref} = \sqrt{2}/2$ m/s. The robot's motion was limited by the dynamic constraints: $v_{\mathcal{R}}^{max} = 1$ m/s, $w_{\mathcal{R}}^{max} = 1$ rad/s, $a_{\mathcal{R}}^{max} = 1$ m/s², $\alpha_{\mathcal{R}}^{max} = 1$ rad/s².

On top of that, $w_{\mathcal{R}}^{max}$ was additionally bounded to balance those three algorithms. Since the mobile robot's motion was controlled by its wheels, we imposed the maximum wheel velocity equal to $v_{\mathcal{R}}^{max}$. Then $w_{\mathcal{R}}^{max}$ was bounded by $(v_{\mathcal{R}}^{max} - \|\mathbf{v}_{\mathcal{R}}\|) / \sqrt{\lambda_{\max}(\mathbf{S}_{\mathcal{R}})}$.

Fig. 7 The resultant paths in the *Line* scenario using **a** No Rotation, **b** Jeon and Lee (2014), and **c** the proposed algorithm. The orange ellipses represent the traces of the robot, and the blue circles indicate those of obstacles until the robot reaches its goal position. The lighter the color of an object is, the older its trace is. **d** The comparison between the paths generated by each of the algorithms, where the black circle and x-mark are the start and goal positions. The red, blue, and green solid lines represent the paths of No Rotation, Jeon and Lee (2014), and the proposed algorithm, respectively (Color figure online)



5.2 Line scenario

An elliptic robot \mathcal{R} and an circular obstacle \mathcal{O} with radius of 0.5 m started at the opposite ends and moved along the same line. At the beginning, \mathcal{R} was stalled at $\mathbf{p}_{\mathcal{R}} = (0 \text{ m}, 0 \text{ m})$ with $\theta_{\mathcal{R}} = 45^\circ$, and \mathcal{O} moved with $\mathbf{v}_{\mathcal{O}} = (-0.5 \text{ m/s}, 0 \text{ m/s})$ at $\mathbf{p}_{\mathcal{O}} = (8 \text{ m}, 0 \text{ m})$. The robot's goal position was equal to $\mathbf{p}_{\mathcal{O}}$.

Figure 7 shows the resultant traces using the three algorithms. The robot in Fig. 7a traveled more distance to avoid \mathcal{O} than those in Fig. 7b, c, where the robot exploited its rotation to decrease the traveled distance. Figure 7d compares the paths for each of the algorithms at the same time. Table 1 shows the numerical results of the simulation. The travel distance of the proposed algorithm was almost the same with that of Jeon and Lee (2014), but 3.11 % shorter than that of No Rotation. Likewise, the travel times of the proposed algorithm and Jeon and Lee (2014) were equal, but theirs are 4.69 % shorter than that of No Rotation. Although the computation time of the proposed algorithm was about three times longer than those of the others, the differences were trivial because they were far shorter than the sampling period Δt .

Table 1 Simulation results in *Line* scenario

Algorithm	Travel distance (m)	Travel time (s)	Computation time (ms)
No rotation	8.322	12.8	0.013
EBVO (2014)	8.068	12.2	0.014
The proposed one	8.063	12.2	0.059

5.3 Multiple moving obstacles scenario

An elliptic robot and three elliptic obstacles were moving in the workspace. Likewise the previous scenario, the robot and an obstacle \mathcal{O}_1 started at the opposite ends and moved along the same line. At the beginning, the robot was halted at $\mathbf{p}_{\mathcal{R}} = (0 \text{ m}, 0 \text{ m})$ with $\theta_{\mathcal{R}} = -100^\circ$. The obstacle \mathcal{O}_1 whose shape matrix was $\begin{bmatrix} 0.2 & -0.2 \\ -0.2 & 0.5 \end{bmatrix}$ moved to the robot with $\mathbf{v}_{\mathcal{O}_1} = (-0.5 \text{ m/s}, -0.5 \text{ m/s})$ at $\mathbf{p}_{\mathcal{O}_1} = (5 \text{ m}, 5 \text{ m})$. The robot's goal position was also the same with the initial position of \mathcal{O}_1 . The other two obstacles, \mathcal{O}_2 and \mathcal{O}_3 , were across the path of the robot and had the same shape matrix $\begin{bmatrix} 0.2 & 0.2 \\ 0.2 & 0.5 \end{bmatrix}$. Initially, the obstacle \mathcal{O}_2 moved with $\mathbf{v}_{\mathcal{O}_2} = (-0.5 \text{ m/s}, 0.5 \text{ m/s})$ at $\mathbf{p}_{\mathcal{O}_2} = (4 \text{ m}, 1 \text{ m})$, and the obstacle \mathcal{O}_3 moved with $\mathbf{v}_{\mathcal{O}_3} = (0.5 \text{ m/s}, -0.5 \text{ m/s})$ at $\mathbf{p}_{\mathcal{O}_3} = (-2 \text{ m}, 10 \text{ m})$.

Figure 8 indicates the simulation result using the proposed algorithm. The resultant traces are shown in Fig. 8a, and the robot's velocities with respect to the time are presented in Fig. 8b–d. Until the robot grazed \mathcal{O}_1 at $t = 2.6 \text{ s}$, the robot aimed the right side of \mathcal{O}_1 and rotated to pass the obstacle with a less traveled distance. From $t = 2.8 \text{ s}$ to $t = 10.4 \text{ s}$, the robot did not rotate because $\mathbf{v}_{\mathcal{R}}^{pref} \in RAV \setminus \partial V\mathcal{O}_{\mathcal{R}}$. In addition, the robot rotated to avoid \mathcal{O}_3 more efficiently because $\mathbf{v}_{\mathcal{R}}^{pref}$ moved to the inside of $V\mathcal{O}_{\mathcal{R}}$ after $t = 10.6 \text{ s}$. Table 2 shows the comparison between the performances of these three algorithms. The travel distance of the proposed algorithm was 6.92 and 9.72 % shorter than those of No Rotation and Jeon and Lee (2014). Also, the travel time of the proposed algorithm was 8.06 and 21.5 % shorter than those of the other

Fig. 8 The simulation result in the *Multiple moving obstacle* scenario using the proposed algorithm. **a** The resultant traces of the robot and three obstacles. The *orange ellipses* represent the traces of the robot, and the *blue ellipses* indicate those of the obstacles until the robot reaches its goal position. **b–d** the robot's linear and angular velocities with respect to the time (Color figure online)

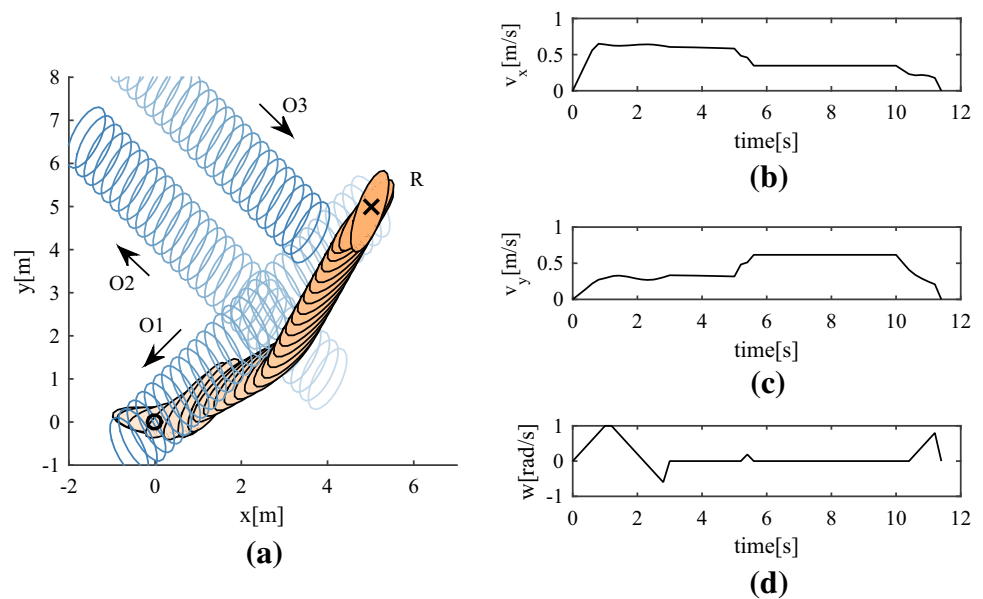


Table 2 Simulation results in *Multiple moving obstacle* scenario

Algorithm	Travel distance (m)	Travel time (s)	Computation time (ms)
No rotation	7.8691	12.4	0.031
EBVO (2014)	8.1130	13.8	0.033
The proposed one	7.3247	11.4	0.080

models, respectively. In addition, all the computation times were still far shorter than the sampling period.

5.4 Pedestrians avoidance scenario

The proposed algorithm was validated using a real-world dataset. The BIWI Walking Pedestrians dataset was video

data of walking students on the campus of ETH Zurich filmed from a bird eye view (Pellegrini et al. 2009), annotated at 2.5 fps. We extracted a sequence about 30 s long, where the total number of the pedestrians was 53 and the maximum number of them crossing at the same time was 18.

In the simulation, each of the pedestrians was represented by an ellipse whose major and minor radii were 40 cm and 20 cm and major axis was perpendicular to its heading direction. The robot was also supposed to an ellipse having the same size of the pedestrians, but it was given a safe margin of 15 cm to compensate the error in assumption that the pedestrians continued their most recent velocity. In addition, the maximum translational and rotational speed limits are assigned to $v_{\mathcal{R}}^{\max} = 1.5$ m/s and $w_{\mathcal{R}}^{\max} = 1$ rad/s, but there is no limit on the accelerations. The robot was initially located at one side of the walkway and moved to the opposite side

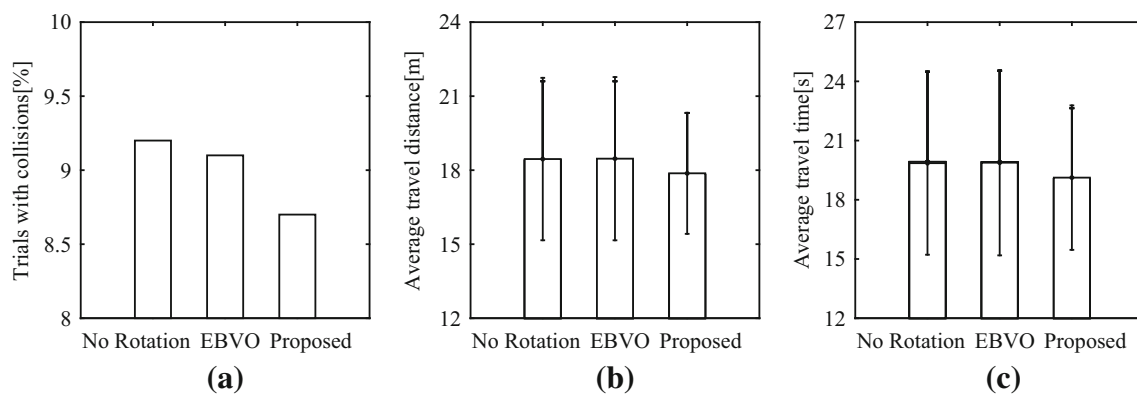


Fig. 9 Simulation results in the *Pedestrians avoidance* scenario. The simulation results of three algorithms for 1000 runs were compared with respect to **a** the percentage of the trials with collision, **b** the average travel distance, and **c** the average travel time. The distances and

times were calculated for the 861 runs where the robot successfully reached the goal with all the algorithms and were represented by bar plots with *error bars* of one standard deviation

while avoiding the pedestrians. The algorithms were tested in 1,000 repeated runs, where the initial and goal position of the robot were randomly chosen.

The simulation results are presented in Fig. 9. Figure 9a indicates the percentage of runs where the robot failed to avoid collisions with the pedestrians. Here the proposed algorithm shows the highest success rate among the three algorithms because it exploited the robot's rotation to efficiently avoid the obstacles. In Fig. 9b, c, the average travel distances and times were calculated over the runs where the robot successfully reached the goal with all the algorithms for the sake of fairness. As a result, the travel distance of the proposed algorithm was 3.23 and 3.32 % shorter than those of No Rotation and Jeon and Lee (2014). Also, the travel time of the proposed algorithm was 3.84 and 3.96 % shorter than those of the others, respectively.

6 Conclusion

This paper has suggested a local collision avoidance algorithm for a holonomic elliptic robot, decomposed into two parts: linear and angular motion planning.

In the first part, the new linear velocity of a non-rotating elliptic robot was selected in order to generate a trajectory to the goal without collision with obstacles. To this end, the tangent lines of the C-obstacle of an elliptic obstacle with respect to an elliptic robot were first derived. Next, it was shown that the set of robot's linear velocities that would induce a collision with the obstacle within a finite time horizon, called EBVO, was bounded by three tangent lines of the C-obstacle. As a result, the robot did not collide with obstacles by selecting its linear velocity outside of the EBVO.

In the second part, the new angular velocity of the robot moving with the linear velocity from the first part was selected due to avoid obstacles with a less traveled distance. The collision-free rotation angles were first derived. Next, the preferred angular velocities at which the robot potentially circumvented obstacles with the minimum possible deviation were calculated. Consequently, the robot could avoid obstacles efficiently by changing its orientation safely. From the simulations, it was demonstrated that the robot utilizing the proposed algorithm avoided obstacles with a less traveled distance and time than those using the other algorithms.

In the future work, the proposed algorithm needs to be extended to consider the reciprocity between robots because it is not applicable in multi-robot environments. Also, it is planned to study the kinematic constraints of non-holonomic robots to expand the application area of the proposed algorithm.

Acknowledgements This research was supported by a grant to Bio-Mimetic Robot Research Center Funded by Defense Acquisition

Program Administration, and by Agency for Defense Development (UD130070ID).

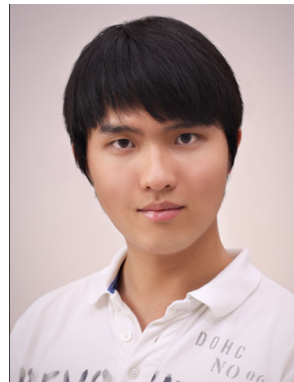
References

- Alonso-Mora, J., Naegeli, T., Siegwart, R., & Beardsley, P. (2015). Collision avoidance for aerial vehicles in multi-agent scenarios. *Autonomous Robots*, 39(1), 101–121. doi:[10.1007/s10514-015-9429-0](https://doi.org/10.1007/s10514-015-9429-0).
- Chakravarthy, A., & Ghose, D. (1998). Obstacle avoidance in a dynamic environment: A collision cone approach. *IEEE Transactions on Systems, Man, and Cybernetics Part A: Systems and Humans*, 28(5), 562–574. doi:[10.1109/3468.709600](https://doi.org/10.1109/3468.709600).
- Chakravarthy, A., & Ghose, D. (2011). Generalization of the collision cone approach for motion safety in 3-D environments. *Autonomous Robots*, 32(3), 243–266. doi:[10.1007/s10514-011-9270-z](https://doi.org/10.1007/s10514-011-9270-z).
- Choi, Y. K., Liu, Y., & Kim, M. S. (2006). Continuous collision detection for two moving elliptic disks. *IEEE Transactions on Robotics*, 22(2), 213–224. doi:[10.1109/TRO.2005.862479](https://doi.org/10.1109/TRO.2005.862479).
- Choi, Y. K., Chang, J. W., Wang, W., Kim, M. S., & Elber, G. (2009). Continuous collision detection for ellipsoids. *IEEE Transactions on Visualization and Computer Graphics*, 15(2), 311–325. doi:[10.1109/TVCG.2008.80](https://doi.org/10.1109/TVCG.2008.80).
- Etayo, F., Gonzalez-Vega, L. del Rio, N. (2006). A new approach to characterizing the relative position of two ellipses depending on one parameter. *Computer Aided Geometric Design*, 23(4), 324–350. doi:[10.1016/j.cagd.2006.01.002](https://doi.org/10.1016/j.cagd.2006.01.002).
- Fiorini, P., & Shiller, Z. (1993). Motion planning in dynamic environments using the relative velocity paradigm. *IEEE International Conference on Robotics and Automation* (Vol. 1, pp. 560–566). Atlanta, GA: IEEE. doi:[10.1109/ROBOT.1993.292038](https://doi.org/10.1109/ROBOT.1993.292038).
- Fiorini, P., & Shiller, Z. (1998). Motion planning in dynamic environments using velocity obstacles. *International Journal of Robotics Research*, 17(7), 760–772. doi:[10.1177/027836499801700706](https://doi.org/10.1177/027836499801700706).
- Fujimura, K., & Samet, H. (1989). Time-minimal paths among moving obstacles. In: *IEEE International Conference on Robotics and Automation (ICRA)* (pp. 1110–1115). Scottsdale, AZ: IEEE. doi:[10.1109/ROBOT.1989.100129](https://doi.org/10.1109/ROBOT.1989.100129).
- Fujimura, K., & Samet, H. (1993). Planning a time-minimal motion among moving obstacles. *Algorithmica*, 10(1), 41–63. doi:[10.1007/BF01908631](https://doi.org/10.1007/BF01908631).
- Giese, A., Latypov, D., & Amato, N. M. (2014). Reciprocally-rotating velocity obstacles. In: *2014 IEEE International Conference on Robotics and Automation* (pp. 3234–3241). Hong Kong: IEEE. doi:[10.1109/ICRA.2014.6907324](https://doi.org/10.1109/ICRA.2014.6907324).
- Goerzen, C., Kong, Z., & Mettler, B. (2010). A survey of motion planning algorithms from the perspective of autonomous uav guidance. *Journal of Intelligent and Robotic Systems: Theory and Applications*, 57(1–4), 65–100. doi:[10.1007/s10846-009-9383-1](https://doi.org/10.1007/s10846-009-9383-1).
- Guy, S. J., Chhugani, J., Kim, C., Satish, N., Lin, M., Manocha, D., Dubey, P. (2009). ClearPath: Highly parallel collision agent simulation. In: *ACM SIGGRAPH/Eurographics Symposium on Computer Animation-SCA '09* (pp. 177–187). New Orleans, LA: ACM Press. doi:[10.1145/1599470.1599494](https://doi.org/10.1145/1599470.1599494).
- Jeon, J. D., & Lee, B. H. (2014). Ellipse-based velocity obstacles for local navigation of holonomic mobile robot. *Electronics Letters*, 50(18), 1279–1281. doi:[10.1049/el.2014.1592](https://doi.org/10.1049/el.2014.1592).
- Jia, X., Choi, Y. K., Mourrain, B., & Wang, W. (2011). An algebraic approach to continuous collision detection for ellipsoids. *Computer Aided Geometric Design*, 28(3), 164–176. doi:[10.1016/j.cagd.2011.01.004](https://doi.org/10.1016/j.cagd.2011.01.004).
- John, F. (2014). Extremum problems with inequalities as subsidiary conditions. In G. Giorgi & T. H. Kjeldsen (Eds.), *Traces and emergence of nonlinear programming* (pp. 197–215). Basel: Springer.

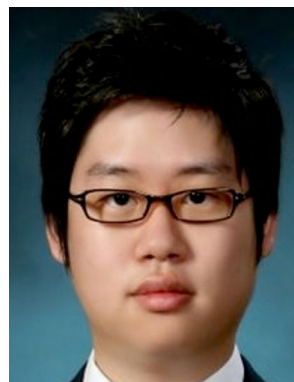
- Ju, MY., Liu, JS., Shiang, SP., Chien, YR., Hwang, KS., Lee, WC. (2001). A novel collision detection method based on enclosed ellipsoid. In: *Proceedings 2001 ICRA. IEEE International Conference on Robotics and Automation (Cat. No.01CH37164)* (Vol. 3, pp. 2897–2902). Seoul: IEEE. doi:[10.1109/ROBOT.2001.933061](https://doi.org/10.1109/ROBOT.2001.933061).
- Karamouzas, I., Guy, SJ. (2015). Prioritized group navigation with formation velocity obstacles. In: *IEEE International Conference on Robotics and Automation (ICRA)* (Vol. 2015, pp. 5983–5989). IEEE. doi:[10.1109/ICRA.2015.7140038](https://doi.org/10.1109/ICRA.2015.7140038).
- Lennerz, C., Schomer, E. (2002). Efficient distance computation for quadratic curves and surfaces. In: *Geometric modeling and processing, 2002. Proceedings* (pp. 60–69). doi:[10.1109/GMAP.2002.1027497](https://doi.org/10.1109/GMAP.2002.1027497).
- Lozano-Pérez, T. (1983). Spatial planning: A configuration space approach. *IEEE Transactions on Computers C*, 32(2), 108–120. doi:[10.1109/TC.1983.1676196](https://doi.org/10.1109/TC.1983.1676196).
- Miloh, T. (1983). Game of two elliptical ships. *Optimal Control Applications and Methods*, 4(1), 13–29.
- Moler, C. B. (1991). ROOTS-of polynomials, that is. *The MathWorks Newsletter*, 5(1), 8–9.
- Moler, C. B., & Stewart, G. W. (1973). An algorithm for generalized matrix eigenvalue problems. *SIAM Journal on Numerical Analysis*, 10(2), 241–256. doi:[10.1137/0710024](https://doi.org/10.1137/0710024).
- Pellegrini, S., Ess, A., Schindler, K., van Gool, L. (2009). You'll never walk alone: Modeling social behavior for multi-target tracking. In: *2009 IEEE 12th International Conference on Computer Vision* (pp. 261–268). Kyoto: IEEE. doi:[10.1109/ICCV.2009.5459260](https://doi.org/10.1109/ICCV.2009.5459260).
- Rimon, E., & Boyd, S. P. (1997). Obstacle collision detection using best ellipsoid fit. *Journal of Intelligent and Robotic Systems: Theory and Applications*, 18(2), 105–126.
- Sohn, KA., Juttler, B., Kim, MS., Wang, W. (2002). Computing distances between surfaces using line geometry. In: *Computer Graphics and Applications, 2002. Proceedings 10th Pacific Conference on* (pp. 236–245). doi:[10.1109/PCCGA.2002.1167866](https://doi.org/10.1109/PCCGA.2002.1167866).
- Takahashi, M., Suzuki, T., Matsumura, T., & Yorozu, A. (2013). Dynamic obstacle avoidance with simultaneous translational and rotational motion control for autonomous mobile robot. In J. L. Ferrier, A. Bernard, O. Gusikhin, & K. Madani (Eds.), *Informatics in control, automation and robotics* (pp. 51–64). Lecture notes in electrical engineering Berlin: Heidelberg. doi:[10.1007/978-3-642-31353-0](https://doi.org/10.1007/978-3-642-31353-0).
- Van Den Berg, J., Lin, M., Manocha, D. (2008). Reciprocal velocity obstacles for real-time multi-agent navigation. In: *IEEE International Conference on Robotics and Automation (ICRA)* (pp. 1928–1935). Pasadena, CA: IEEE. doi:[10.1109/ROBOT.2008.4543489](https://doi.org/10.1109/ROBOT.2008.4543489).
- Van Den Berg, J., Guy, S. J., Lin, M., & Manocha, D. (2011). Reciprocal n-body collision avoidance. In C. Pradalier, R. Siegwart, & G. Hirzinger (Eds.), *Robotics research, springer tracts in advanced robotics* (pp. 3–19). Heidelberg: Springer.
- Wang, W., Wang, J., & Kim, M. S. (2001). An algebraic condition for the separation of two ellipsoids. *Computer Aided Geometric Design*, 18(6), 531–539. doi:[10.1016/S0167-8396\(01\)00049-8](https://doi.org/10.1016/S0167-8396(01)00049-8).
- Wang, W., Choi, YK., Chan, B., Kim, MS., Wang, J. (2004). Efficient collision detection for moving ellipsoids using separating planes. In: *Computing* (Vol. 72, pp. 235–246). New York.
- Zheng, X., & Palfy-Muhoray, P. (2007). Distance of closest approach of two arbitrary hard ellipses in two dimensions. *Physical Review E*, 75(6), 1–6. doi:[10.1103/PhysRevE.75.061709](https://doi.org/10.1103/PhysRevE.75.061709).



Beom H. Lee received the B.S. degree and M.S. degree in electronics engineering from Seoul National University, Seoul, the Republic of Korea in 1978 and 1980, respectively, and the Ph.D. degree in computer, information, and control engineering from the University of Michigan, Ann Arbor, MI in 1985. He was an Assistant Professor with the School of Electrical Engineering at Purdue University, West Lafayette, IN from 1985 to 1987. He joined Seoul National University in 1987, and is currently a Professor with the Department of Electrical and Computer Engineering. His research interests include multi-agent system coordination, control, and application. Prof. Lee has been a Fellow of the Robotics and Automation Society since 2004.



Jae D. Jeon received the B.S. degree in electrical engineering from Seoul National University, Seoul, the Republic of Korea in 2011, where he is currently working toward the Ph.D. degree with the Department of Electrical and Computer Engineering. His current research interests include multi-agent system cooperation, multi-robot formation control, and collision avoidance.



Jung H. Oh received the B.S. and M.S. degrees in electrical engineering and computer science from Seoul National University, Seoul, Korea in 2012 and 2014. He is currently a Ph. D. candidate in the Department of Electrical and Computer Engineering at Seoul National University. His research interests include vision-based robotics applications, machine learning, and multi-agent system coordination.